

DRAFT VERSION JANUARY 24, 2023
Typeset using L^AT_EX twocolumn style in AASTeX631

CEERS Spectroscopic Confirmation of NIRC*am*-Selected $z \gtrsim 8$ Galaxy Candidates with *JWST*/NIRSpec: Initial Characterization of their Properties

SEIJI FUJIMOTO,^{1,*} PABLO ARRABAL HARO,² MARK DICKINSON,² STEVEN L. FINKELSTEIN,¹ JEYHAN S. KARTALTEPE,³
REBECCA L. LARSON,^{1,†} DENIS BURGARELLA,⁴ MICAELA B. BAGLEY,¹ PETER BEHROOZI,^{5,6} KATHERINE CHWOROWSKY,^{1,†}
MICHAELA HIRSCHMANN,^{7,8} JONATHAN R. TRUMP,⁹ STEPHEN M. WILKINS,^{10,11} L. Y. AARON YUNG,^{12,‡}
ANTON M. KOEKEMOER,¹³ CASEY PAPOVICH,^{14,15} NOR PIRZKAL,¹⁶ HENRY C. FERGUSON,¹³ ADRIANO FONTANA,¹⁷
NORMAN A. GROGIN,¹³ ANDREA GRAZIAN,¹⁸ LISA J. KEWLEY,¹⁹ DALE D. KOCEVSKI,²⁰ JENNIFER M. LOTZ,²¹
LAURA PENTERICCI,¹⁷ SWARA RAVINDRANATH,¹³ RACHEL S. SOMERVILLE,²² RICARDO O. AMORÍN,^{23,24}
BREN E. BACKHAUS,⁹ ANTONELLO CALABRÒ,¹⁷ CAITLIN M. CASEY,¹ M. C. COOPER,²⁵ MAXIMILIEN FRANCO,¹
MAURO GIAVALISCO,²⁶ NIMISH P. HATHI,¹³ SANTOSH HARISH,³ TAYLOR A. HUTCHISON,^{12,‡} KARTHEIK G. IYER,²⁷
INTAE JUNG,¹³ RAY A. LUCAS,¹³ AND JORGE A. ZAVALA⁶

¹*Department of Astronomy, The University of Texas at Austin, Austin, TX, USA*

²*NSF's National Optical-Infrared Astronomy Research Laboratory, 950 N. Cherry Ave., Tucson, AZ 85719, USA*

³*Laboratory for Multiwavelength Astrophysics, School of Physics and Astronomy, Rochester Institute of Technology, 84 Lomb Memorial Drive, Rochester, NY 14623, USA*

⁴*Aix Marseille Univ, CNRS, CNES, LAM Marseille, France*

⁵*Department of Astronomy and Steward Observatory, University of Arizona, Tucson, AZ 85721, USA*

⁶*Division of Science, National Astronomical Observatory of Japan, 2-21-1 Osawa, Mitaka, Tokyo 181-8588, Japan*

⁷*Institute for Physics, Laboratory for Galaxy Evolution and Spectral modelling, Ecole Polytechnique Fédérale de Lausanne, Observatoire de Sauverny, Chemin Pegasi 51, 1290 Versoix, Switzerland*

⁸*INAF, Osservatorio Astronomico di Trieste, Via Tiepolo 11, 34131 Trieste, Italy*

⁹*Department of Physics, 196 Auditorium Road, Unit 3046, University of Connecticut, Storrs, CT 06269, USA*

¹⁰*Astronomy Centre, University of Sussex, Falmer, Brighton BN1 9QH, UK*

¹¹*Institute of Space Sciences and Astronomy, University of Malta, Msida MSD 2080, Malta*

¹²*Astrophysics Science Division, NASA Goddard Space Flight Center, 8800 Greenbelt Rd, Greenbelt, MD 20771, USA*

¹³*Space Telescope Science Institute, 3700 San Martin Drive, Baltimore, MD 21218, USA*

¹⁴*Department of Physics and Astronomy, Texas A&M University, College Station, TX, 77843-4242 USA*

¹⁵*George P. and Cynthia Woods Mitchell Institute for Fundamental Physics and Astronomy, Texas A&M University, College Station, TX, 77843-4242 USA*

¹⁶*ESA/AURA Space Telescope Science Institute*

¹⁷*INAF Osservatorio Astronomico di Roma, Via Frascati 33, 00078 Monte Porzio Catone, Rome, Italy*

¹⁸*INAF-Osservatorio Astronomico di Padova, Vicolo dell'Osservatorio 5, I-35122, Padova, Italy*

¹⁹*Harvard-Smithsonian Center for Astrophysics, 60 Garden Street, Cambridge, MA 02138, USA*

²⁰*Department of Physics and Astronomy, Colby College, Waterville, ME 04901, USA*

²¹*Gemini Observatory/NSF's National Optical-Infrared Astronomy Research Laboratory, 950 N. Cherry Ave., Tucson, AZ 85719, USA*

²²*Center for Computational Astrophysics, Flatiron Institute, 162 5th Avenue, New York, NY 10010, USA*

²³*Instituto de Investigación Multidisciplinar en Ciencia y Tecnología, Universidad de La Serena, Raul Bitrán 1305, La Serena 2204000, Chile*

²⁴*Departamento de Astronomía, Universidad de La Serena, Av. Juan Cisternas 1200 Norte, La Serena 1720236, Chile*

²⁵*Department of Physics & Astronomy, University of California, Irvine, 4129 Reines Hall, Irvine, CA 92697, USA*

²⁶*University of Massachusetts Amherst, 710 North Pleasant Street, Amherst, MA 01003-9305, USA*

²⁷*Dunlap Institute for Astronomy & Astrophysics, University of Toronto, Toronto, ON M5S 3H4, Canada*

Submitted to ApJL

Corresponding author: Seiji Fujimoto
fujimoto@utexas.edu

ABSTRACT

We present *JWST* NIRSpec spectroscopy for 11 galaxy candidates with photometric redshifts of $z \simeq 9\text{--}13$ and $M_{\text{UV}} \in [-21, -18]$ newly identified in NIRC*am* images in the Cosmic Evolution Early Release Science (CEERS) Survey. We confirm emission line redshifts for 7 galaxies at $z = 7.762\text{--}8.998$ using spectra at $\sim 1\text{--}5\mu\text{m}$ either with the NIRSpec prism or its three medium resolution ($R \sim 1000$) gratings. For $z \simeq 9$ photometric candidates, we achieve a high confirmation rate of $\simeq 90\%$, which validates the classical dropout selection from NIRC*am* photometry. No robust emission lines are identified in three galaxy candidates at $z > 10$, where the strong [OIII] and H β lines would be redshifted beyond the wavelength range observed by NIRSpec, and the Lyman- α continuum break is not detected with the sensitivity of the current data. Compared with *HST*-selected bright galaxies ($M_{\text{UV}} \simeq -22$) that are similarly spectroscopically confirmed at $z \gtrsim 8$, these NIRC*am*-selected galaxies are characterized by lower star formation rates ($\text{SFR} \simeq 4 M_{\odot} \text{ yr}^{-1}$) and lower stellar masses ($\simeq 10^8 M_{\odot}$), but with higher specific SFR ($\simeq 40 \text{ Gyr}^{-1}$), higher [OIII]+H β equivalent widths ($\simeq 1100\text{\AA}$), and elevated production efficiency of ionizing photons ($\log(\xi_{\text{ion}}/\text{Hz erg}^{-1}) \simeq 25.8$) induced by young stellar populations ($< 10 \text{ Myrs}$) accounting for $\simeq 20\%$ of the galaxy mass, highlighting the key contribution of faint galaxies to cosmic reionization. Taking advantage of the homogeneous selection and sensitivity, we also investigate metallicity and ISM conditions with empirical calibrations using the [OIII]₅₀₀₈/H β ratio. We find that galaxies at $z \sim 8\text{--}9$ have higher SFRs and lower metallicities than galaxies at similar stellar masses at $z \sim 2\text{--}6$, which is generally consistent with the current galaxy formation and evolution models.

Keywords: Early universe (435); Galaxy formation (595); Galaxy evolution (594); High-redshift galaxies (734)

1. INTRODUCTION

Studying early galaxies is key to understanding fundamental cosmological questions such as the development of large-scale structure, dark matter, and the processes that govern cosmic reionization and early galaxy formation and evolution. In the last decades, the search for galaxies seen within the epoch of Reionization (EoR) has been successful at $6 \lesssim z \lesssim 11$. With thousands of galaxies discovered, deep *Hubble Space Telescope* (*HST*) surveys have provided valuable demographic data for these galaxies, including an initial characterization of the stellar component, in terms of un-obscured star formation rates and sizes (e.g., Ellis et al. 2013; Bouwens et al. 2015; Finkelstein et al. 2015; Oesch et al. 2016; Bhatawdekar et al. 2019).

The start of *James Webb Space Telescope* (*JWST*) operations (Rigby et al. 2022) has led to significant progress in the discovery and investigation of galaxies at very early cosmic epochs. From the Early Release Observations (ERO; Pontoppidan et al. 2022) and the Early Release Science programs (ERS; e.g., Treu et al. 2022; Finkelstein et al. 2022b), multiple NIRC*am* imaging surveys have been carried out towards both lensing

clusters and blank fields, where dozens of high-redshift galaxy candidates have been identified at $z \simeq 9\text{--}17$ (e.g., Adams et al. 2022; Atek et al. 2022; Bouwens et al. 2022b; Bradley et al. 2022; Castellano et al. 2022; Donnan et al. 2022b; Finkelstein et al. 2022a,b; Harikane et al. 2022; Labbe et al. 2022; Morishita & Stiavelli 2022; Naidu et al. 2022b; Yan et al. 2022). Their abundance at the bright-end ($M_{\text{UV}} \lesssim -20$) exceeds nearly all theoretical predictions so far (e.g., Behroozi & Silk 2015; Dayal et al. 2017; Yung et al. 2019a, 2020a; Behroozi et al. 2019, 2020; Davé et al. 2019; Wilkins et al. 2022b,a; Kannan et al. 2022; Mason et al. 2022), suggesting several possibilities, including that star formation in early systems is dominated by a top-heavy initial mass function (IMF), complete lack of dust attenuation, and/or changing star-formation physics (e.g., Harikane et al. 2022; Finkelstein et al. 2022b; Ferrara et al. 2022; Boylan-Kolchin 2022; Lovell et al. 2022; Menci et al. 2022).

Deep ALMA follow-up observations have been immediately performed through Director’s Discretionary Time (DDT) for several remarkably bright ($M_{\text{UV}} \in [-22, -21]$) *JWST* galaxy candidates at $z \sim 11\text{--}17$ (e.g., Castellano et al. 2022; Naidu et al. 2022b; Harikane et al. 2022), showing no robust dust continuum detection from any of these candidates (Bakx et al. 2022; Yoon et al. 2022; Fujimoto et al. 2022a). These ALMA results disfavor the possibility of lower- z dusty interlopers (Fuji-

* Hubble Fellow

† NSF Graduate Fellow

‡ NASA Postdoctoral Fellow

moto et al. 2022a), although spectroscopic confirmation of these sources is inevitably required.

In this paper, we present *JWST*/NIRSpec results of follow-up observations of $z \gtrsim 9$ galaxy candidates identified in the first epoch of the Cosmic Evolution Early Release Science (CEERS) Survey. This is the first homogeneous, luminosity-selected follow-up spectroscopy for *JWST* high-redshift galaxy candidates at $z \gtrsim 9$ in the UV luminosity range of $M_{UV} \in [-21, -18]$. This sets the benchmark for the spectroscopic confirmation of large samples of galaxies, further allowing detailed investigations into the UV luminosity function shape at $z \gtrsim 9$ and the characterization of the high-redshift Lyman-break galaxy (LBG) population newly identified with *JWST*. This work is complementary to the recent successful spectroscopic confirmation of the higher redshift, but much (1–2 mag) fainter galaxies at $z = 9.51 - 13.20$ in lensing cluster fields (Roberts-Borsani et al. 2022; Williams et al. 2022) or very deep observations of the Hubble Ultra Deep Field (Robertson et al. 2022; Curtis-Lake et al. 2022).

The structure of this paper is as follows. In Section 2, we describe the observations and the data reduction of CEERS *JWST* NIRCам and NIRSpec observations. Section 3 outlines the methods of redshift determination. In Section 4, we present and discuss the results of the validity of the redshift determination and the physical properties for the spectroscopically confirmed sources. A summary of this study is presented in Section 5. Throughout this paper, we assume a flat universe with $\Omega_m = 0.3$, $\Omega_\Lambda = 0.7$, and $H_0 = 70 \text{ km s}^{-1} \text{ Mpc}^{-1}$ and the Chabrier (2003) initial mass function (IMF). We adopt vacuum rest-frame wavelengths for the emission lines. When we show lensed galaxies taken from the literature for comparison, we show the intrinsic properties after magnification corrections.

2. OBSERVATIONS & DATA PROCESSING

The *JWST*/NIRCам (Rieke et al. 2003, 2005; Beichman et al. 2012) and *JWST*/NIRSpec (Jakobsen et al. 2022) data employed in this work were taken as part of the Cosmic Evolution Early Release Science Survey (CEERS; ERS 1345, PI: S. Finkelstein) in the CANDELS (Grogin et al. 2011; Koekemoer et al. 2011) Extended Groth Strip (EGS) field. The complete details of the CEERS program will be presented in Finkelstein et al., (in prep.).

2.1. *JWST*/NIRCам data and Target Selection

The galaxies discussed in this work are part of the photometrically-selected $z \gtrsim 9$ candidate galaxy sample assembled by Finkelstein et al. (2022b). These

galaxy candidates were selected from the CEERS epoch 1 (June 2022) NIRCам imaging data, which are described in full in Bagley et al. (2022). The Finkelstein et al. (2022b) photometry catalog includes measurements over the full NIRCам wavelength range in the F115W, F150W, F200W, F277W, F356W, F410M and F444W filters, which have exposures of ~ 3000 seconds per filter (~ 6000 s for F115W); as well as in the existing *HST*/CANDELS ACS and WFC3 F606W, F814W, F105W, F125W, F140W and F160W bands.

Robust candidate $z \gtrsim 9$ galaxies were selected based on a combination of detection significance and photometric redshift distribution criteria, designed to select well-measured astrophysical sources with photometric redshifts highly likely to be at $z > 8.5$. This full sample consists of 26 candidate galaxies, with the full details available in Finkelstein et al. (2022b). The NIRSpec multi-object spectroscopy (MOS) configurations were designed to maximize the number of these candidates observed, resulting in a total of 11 $z > 8.5$ targets. In Figure 1, we present the source positions of the full 26 candidates and the 11 targets included in the NIRSpec observations. The target properties are summarized in Table 1.

2.2. *JWST*/NIRSpec data

The $z \gtrsim 9$ candidates presented in this work are included in the NIRSpec MOS configurations taken with the Micro Shutter Array (MSA; Ferruit et al. 2022) during the CEERS epoch 2 observations (December 2022). These NIRSpec observations are split into 6 different MSA pointings, each of them observed with the G140M/F100LP, G235M/F170LP and G395M/F290LP medium resolution ($R \approx 1000$; here denoted by “M”) gratings plus the prism ($R \approx 30 - 300$), fully covering the $\sim 1 - 5 \mu\text{m}$ wavelength range. The MSA was configured to use 3-shutter slitlets, enabling a 3-point nodding pattern, shifting the pointing by a shutter length in each direction for background subtraction. The total exposure time per disperser is 3107 s distributed as three integrations (one per nod) of 14 groups each in the NR-SIRS2 readout mode.

The M grating and prism observations have different MSA configurations and so not all targets are observed in both modes. We present spectra of 11 candidates at $z \gtrsim 9$ in this study: 7 were observed with the prism, 5 were observed with the M gratings, and two were observed with both modes (see Table 1).

2.3. NIRSpec data reduction

The details of the CEERS NIRSpec data processing will be presented in Arrabal Haro et al., (in prep.). We

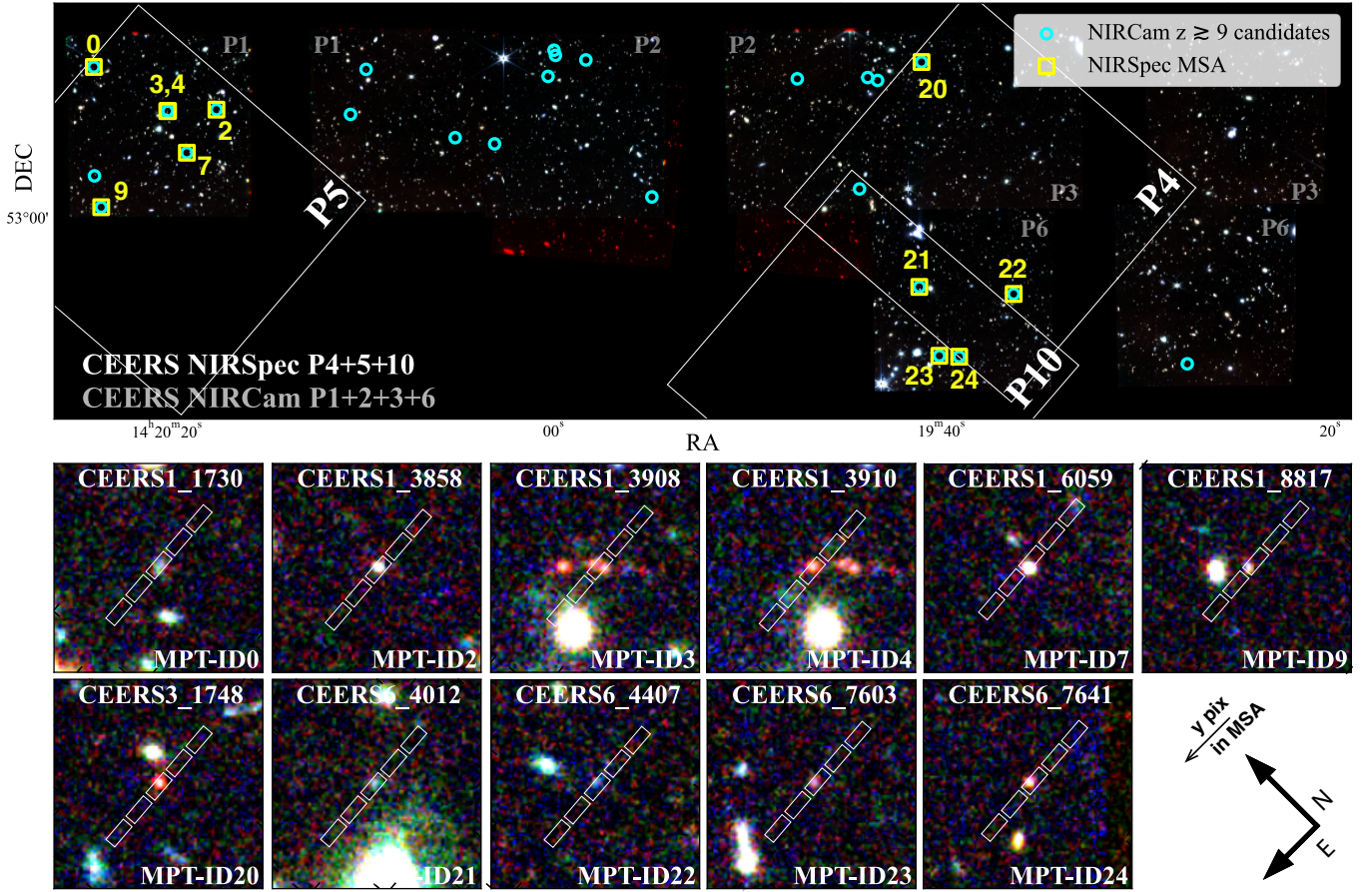


Figure 1. *Top:* A NIRCам RGB color (R: F444W, G: F356W, B: F277W) mosaic combining the NIRCам pointing IDs of 1, 2, 3, and 6 taken in CEERS epoch 1 (June 2022). The white squares show the NIRSpect MSA footprints of the NIRSpect pointing IDs of 4, 5, and 10 taken in CEERS epoch 2 (December 2022). The cyan circles denote the NIRCам-selected high-redshift galaxy candidates at $z \gtrsim 9$ presented in Finkelstein et al. (2022b). The yellow squares represent the NIRSpect MSA targets, and their MPT IDs are labeled. Two candidates in the MSA footprints did not receive slits due to the constraints of the MSA configuration. *Bottom:* RGB $3''.6 \times 3''.6$ image cutouts around the MSA targets (R: F356W, G: F277W, B: F150W). The rectangles show the $0''.2 \times 0''.46$ shutter configuration. We use the standard 3-shutter MSA slitlets and perform a 3-point nodding. Thus, five shutter positions are presented, including the nod positions, which is reflected in the 2D spectra in Figure 2.

summarize the main steps of the reduction here. The NIRSpect data is processed with the STScI Calibration Pipeline¹ version 1.8.5 and the Calibration Reference Data System (CRDS) mapping 1027. We make use of the `calwebb_detector1` pipeline module to subtract the bias and the dark current, correct the $1/f$ noise and generate count-rate maps (CRMs) from the uncalibrated images. At this stage, the parameters of the `jump` step are modified for an improved correction of the “snowball” events² associated with high-energy cosmic rays.

¹ <https://jwst-pipeline.readthedocs.io/en/latest/index.html>

² <https://jwst-docs.stsci.edu/data-artifacts-and-features/snowballs-and-shower-artifacts>

The resulting CRMs are then processed with the `calwebb_spec2` pipeline module which creates two-dimensional (2D) cutouts of the slitlets, performs the background subtraction making use of the 3-nod pattern, corrects the flat-fields, implements the wavelength and photometric calibrations and resamples the 2D spectra to correct the distortion of the spectral trace. The `pathloss` step accounting for the slit loss correction is turned off at this stage of the reduction process. Instead, when required for the analysis, we introduce slit loss corrections based on the morphology of the sources in the NIRCам bands and the location of the slitlet hosting them.

The images of the three nodes are combined at the `calwebb_spec3` pipeline stage, making use of customized apertures for the extraction of the one-dimensional (1D)

Table 1. NIRSpec follow-up targets identified with NIRCcam at $z \sim 9 - 13$

Source Name	MPT-ID	R.A. (deg)	Dec. (deg)	m_{F277W} (mag)	z_{phot}	z_{spec}	S/N	Mode
(1)	(2)	(3)	(4)	(5)	(6)	(7)	(8)	(9)
Confirmed								
CEERS1.3858	2	214.994402	52.989379	27.2	$8.95^{+0.15}_{-0.18}$	8.807 ± 0.003	7.5	P
CEERS1.3908	3	215.005189	52.996580	27.3	$9.04^{+1.29}_{-0.06}$	$8.005 \pm 0.001^{\dagger}$	17.5	P
CEERS1.3910	4	215.005365	52.996697	28.0	$9.55^{+1.05}_{-0.39}$	7.9932 ± 0.0006	9.6	M
CEERS1.6059	7	215.011706	52.988303	27.0	$9.01^{+0.06}_{-0.06}$	8.876 ± 0.002	8.9	P,M
CEERS3.1748	20	214.830685	52.887771	28.5	$8.77^{+0.45}_{-1.08}$	7.769 ± 0.003	7.7	P,M
CEERS6.7603	23	214.901252	52.846997	28.9	$11.32^{+0.30}_{-1.74}$	$8.8805 \pm 0.0005^{\dagger}$	9.8	M
CEERS6.7641	24	214.897232	52.843854	28.1	$8.95^{+1.95}_{-0.15}$	$8.9980 \pm 0.0005^{\dagger}$	11.1	M
Not confirmed								
CEERS1.1730	0	215.010022	53.013641	27.7	$13.36^{+0.84}_{-1.08}$	—	—	P
CEERS6.4012	21	214.888127	52.858987	27.6	$8.89^{+0.36}_{-0.36}$	—	—	M
CEERS6.4407	22	214.869661	52.843646	29.0	$10.63^{+0.81}_{-0.57}$	—	—	M
Tenuous								
CEERS1.8817	9	215.043999	52.994302	28.1	$10.60^{+0.42}_{-0.36}$	9.388? or 9.696?	5.7	P

NOTE— (1) Source name in [Finkelstein et al. \(2022b\)](#). (2) Source ID in the NIRSpec MSA configurations. (3) Right ascension (J2000). (4) Declination (J2000). (5) Observed AB total magnitude in the F277W filter. (6) Photometric redshift. (7) Spectroscopic redshift measured from NIRSpec spectroscopy. (8) S/N from the Gaussian+continuum fit for the [O III]5008, 4960 lines. For MPT-ID9, we show the single-line S/N integrated over the 3 pixels around the peak. (9) NIRSpec observation mode (P: prism, M: Medium resolution gratings). (3)–(6) are taken from [Finkelstein et al. \(2022b\)](#).

\dagger These three galaxies have been also reported in [Tang et al. \(2023\)](#).

spectrum. The custom extraction apertures are visually defined for targets presenting high signal-to-noise ratio (S/N) at the continuum or emission lines, which are easily recognizable in the 2D spectra. For those cases where the targets are too faint for a robust visual identification, a 4-pixel extraction aperture is defined around a spatial location estimated from the relative position of the target within its shutter, derived from the MSA configuration.

Finally, the 2D and 1D spectra are simultaneously inspected with the Mosviz visualization tool³ ([Developers et al. 2023](#)) to mask possible remaining hot pixels and other artifacts in the images, as well as the detector gap (when present). Once inspected and masked, the three M gratings are combined into a single spectrum, resampling to a common wavelength array at the overlapping wavelengths and adopting the mean flux at each pixel, weighted by the flux errors.

We test the accuracy of the error spectrum by comparing the normalized median absolute deviation of the science spectrum (masking out emission lines) to the median of the error spectrum. We find that the real data show fluctuations $\sim 1.5\text{--}2\times$ larger than the typical error

value. Thus, we scale the error spectrum up by this scale factor on an object-by-object basis.

3. ANALYSIS

3.1. Line Identification

We systematically analyze the reduced 1D and 2D spectra of the 11 spectroscopically-observed targets to identify emission line and continuum features. From 7 targets (MPT-ID2, 3, 4, 7, 20, 23, 24), we identify at least two emission line features whose wavelength separations and flux ratios match those of the [O III]5008, 4960 emission lines. These line features have $S/N \gtrsim 7$ and $S/N \gtrsim 3$ from the brighter and the fainter doublet line, respectively, based on the integrated pixel S/N over 3-pixels around the peak. In Figure 2, we show the 1D and 2D spectra of these seven targets.

From one additional target (MPT-ID9), a single line feature is observed with $S/N > 5$ at $5.20 \mu\text{m}$, suggesting a potential identification of [O III]5008 at $z = 9.388$ or $H\beta$ at $z = 9.696$. However, no positive signals at the expected wavelengths for the neighboring lines are confirmed in those potential redshift solutions with $H\beta$, [O III]5008, or [O III]4960. This suggests that the neighboring lines are buried in the noise fluctuations or that the $5.20 \mu\text{m}$ line feature is just noise. We thus focus on the first seven sources with at least two significant

³ <https://jdaviz.readthedocs.io/en/latest/mosviz/index.html>

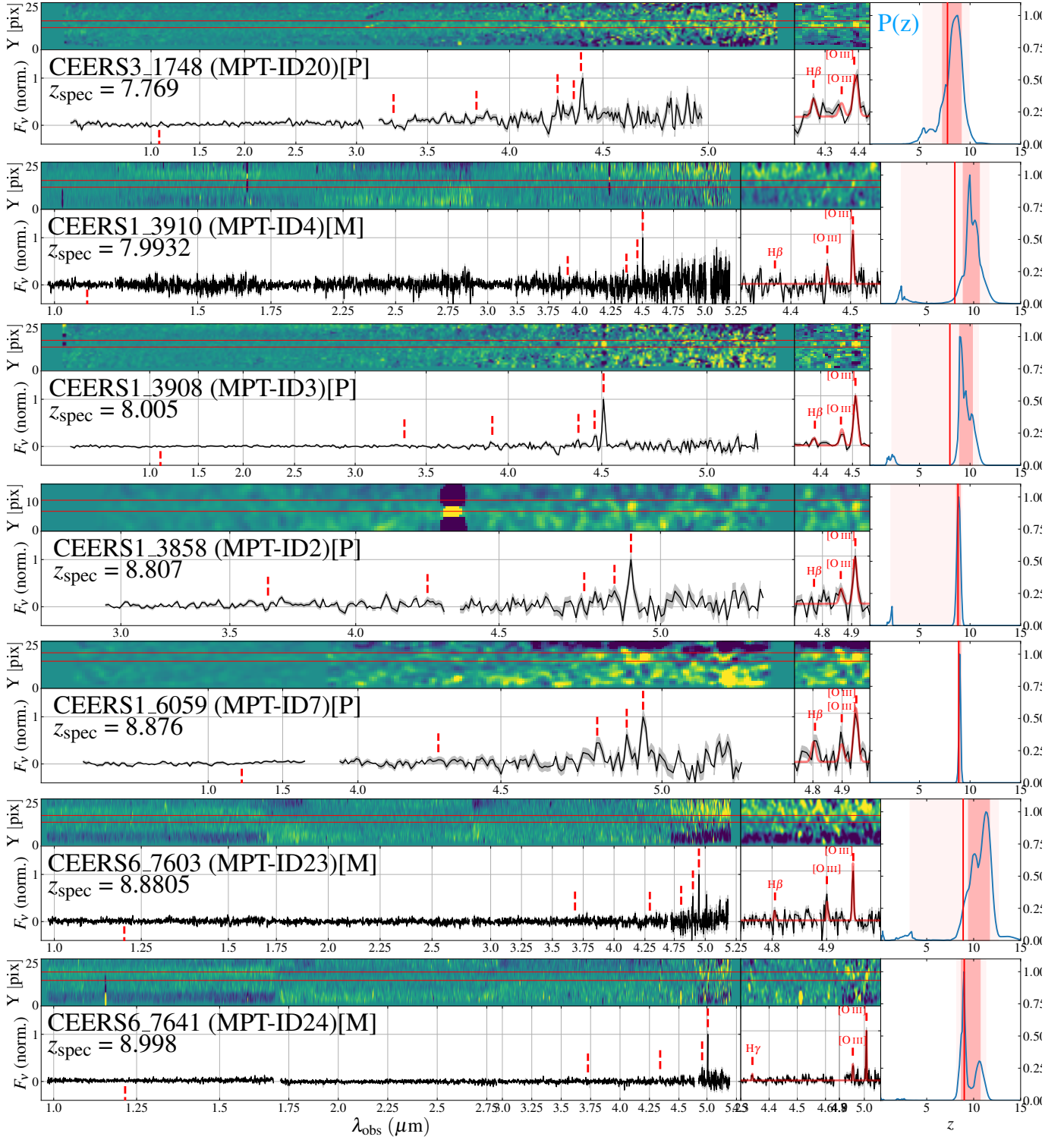


Figure 2. NIRSpect 2D (top) and 1D (bottom) spectra in the observed wavelength frame for the sources that are spectroscopically confirmed. MPT-ID 20, 3, 2, and 7 show the prism spectrum, while ID 4, 23, and 24 show the combined spectra of the G140M, G235M and G395M gratings. The red horizontal lines on the 2D spectrum represent the aperture position used for extracting the 1D spectrum. The red vertical dashed lines denote the expected wavelengths of Ly α , [O II]3727, H γ , H β , [O III]4960, and [O III]5008 from left to right based on our z_{spec} measurement. The 2D spectrum is smoothed with a one-pixel Gaussian kernel. The middle panel shows the zoom-in spectrum around the brightest line feature. The best-fit Gaussian + continuum fit is overlaid on the 1D spectrum. The right panel presents the $P(z)$ as the blue curve, while the red vertical line represents the z_{spec} value. The dark and light red shaded regions indicate 1σ and 2σ ranges of $P(z)$, respectively, from the photometric redshift analysis (Finkelstein et al. 2022b). For sources observed in both the P (prism) and M (medium grating) modes, we show here the spectrum with the better S/N in the brightest emission line.

line features in the following analyses. From the other three targets (MPT-ID0, 21, 22), we identify no secure line or Lyman- α break features. Interestingly, three out of these four potential and non-detected sources are estimated to have $z_{\text{phot}} > 10$ (Finkelstein et al. 2022b), suggesting that these sources might be truly located at $z > 10$, where the typical strong rest-frame optical emission lines ($\text{H}\beta$, $[\text{O III}]5008$, 4960) would lie beyond the red limit of NIRSpec wavelength coverage, making the redshift estimate challenging. The 1D and 2D spectra for these four targets are shown in the Appendix.

3.2. Redshift Measurement

For the seven sources with at least two possible line features, first, we perform template fitting to the NIRSpec 1D spectra to obtain initial redshift estimates. A linear combination of three different CIGALE (Burgarella et al. 2005; Noll et al. 2009; Boquien et al. 2019) models is fitted to the real spectra at a redshift interval, with steps matching the spectral resolution of the grating (or the highest spectral resolution at the red wavelengths in the case of the prism). The templates employed are selected to represent a wide range of galaxy spectra, from emission lines galaxies to quiescent and old massive galaxies. For all the sources spectroscopically confirmed, the best solution from χ^2 minimization over the explored $z = 0-13$ range is consistent with an $[\text{O III}]5008$ detection at long wavelengths.

Using the best-matching template redshifts as the starting estimation, we perform a Gaussian + continuum fitting with a Markov Chain Monte Carlo (MCMC) approach around the peak of the brightest emission line to refine the redshift measurements. Because these prior redshift estimates suggest that the brightest emission line corresponds to $[\text{O III}]5008$ in all seven sources, we adopt the vacuum rest-frame wavelengths of 5008.22 Å and 4960.28 Å for the fit to the brightest and neighboring lines simultaneously by assuming that their line widths and the underlying continuum are the same and the line ratio of 3:1. We determine spectroscopic redshifts in the range $z_{\text{spec}} = 7.7621-8.9979$. We summarize our final z_{spec} measurement and 1σ uncertainty in Table 1. In the right panel of Figure 2, the red line and blue curve show our z_{spec} value compared to the photometric redshift probability distribution $P(z)$ presented in Finkelstein et al. (2022b) based on the photometric SED analysis, respectively. We confirm that the z_{spec} values of all these seven sources are consistent with the $P(z)$ distribution within 2σ . We further discuss the difference between z_{spec} and z_{phot} in Section 4.1. We detect the Lyman- α continuum break only from the prism spectrum of MPT-ID7, where we confirm the wavelength of

the continuum break is consistent with the redshift determined by the emission lines. We show the Lyman- α break observed in MPT-ID7 in the Appendix.

Note that MPT-ID3 and ID4 are separated by less than 3 kpc in physical scale (see Figure 1), and our z_{spec} measurements are $z = 8.005 \pm 0.001$ for ID3 and $z = 7.9932 \pm 0.0006$ for ID4. Although the line feature is less evident in ID4, these independent results suggest that ID3 and ID4 are a close pair and our z_{spec} estimate for ID4 is secure. We also note that the line feature of MPT-ID2 is less clear than other sources in the 2D spectrum. However, we confirm that the S/N increases to 7.5 in the simultaneous fit to both $[\text{O III}]$ lines by fixing the wavelength separation and the line ratio. The z_{spec} value also shows an excellent agreement with z_{phot} . We thus include MPT-ID2 in our z_{spec} sample in this paper.

We also run the template fitting for the remaining four sources in order not to miss the chance that we identify multiple marginal line detections whose wavelength separation matches with a specific redshift solution. However, we do not find any convincing redshift solutions for these sources.

3.3. Line Flux Measurement

We evaluate the fluxes of several key rest-optical emission lines for the z_{spec} sample. We focus on the line fluxes of $[\text{O III}]5008$, $[\text{O III}]4960$, $\text{H}\beta$, and $[\text{O II}]3728$ in this paper. We perform the Gaussian + continuum profile fitting by fixing the redshift. We fit $[\text{O III}]5008$, $[\text{O III}]4960$, and $\text{H}\beta$ lines simultaneously, while we separately fit $[\text{O III}]3727$. In the fitting, we assume the same line width in the velocity frame among these emission lines. We also assume that the same underlying continuum among the $[\text{O III}]5008$, $[\text{O III}]4960$, and $\text{H}\beta$ lines and fix the line ratio of 3:1 between $[\text{O III}]5008$ and $[\text{O III}]4960$. We use the rest-frame 4100–5200 Å for the fit to obtain a stable result for the underlying continuum. For ID24, the wavelength of the $\text{H}\beta$ line falls in the detector gap, while the $\text{H}\gamma$ line is detected at $\text{S/N} \sim 3$. We thus alternatively evaluate the line flux of $\text{H}\gamma$ and convert it to $\text{H}\beta$ with $\text{H}\gamma/\text{H}\beta$ of 0.471 for case B recombination with the electron temperature of 10^4 K without dust correction (Osterbrock 1989) due to the negligible dust extinction estimated from our SED analysis (Section 3.5).

In Table 2, we list the rest-frame equivalent width (EW) values of $[\text{O III}]5008$ and $\text{H}\beta$ and R3 ($\equiv [\text{O III}]5008/\text{H}\beta$). When we do not securely constrain the $\text{H}\beta$ flux more than $\text{S/N} = 2$, we place the conservative 3σ upper and lower limits for $\text{EW}(\text{H}\beta)$ and R3, respectively. When the continuum is not well constrained ($\text{S/N} < 2$) from the fit, we estimate the underlying con-

Table 2. Physical Properties of the NIRCам CEERS galaxies confirmed at $z_{\text{spec}} \simeq 8 - 9$

MPT-ID	z_{spec}	M_{UV} (mag)	$E(B - V)$ (mag)	SFR ($M_{\odot} \text{ yr}^{-1}$)	M_{star} ($10^8 M_{\odot}$)	f_{burst}	EW([OIII]5007) (Å)	EW(H β) (Å)	R3	O32	Mode
(1)	(2)	(3)	(4)	(5)	(6)	(7)	(8)	(9)	(10)	(11)	(12)
2	8.807	-20.44	$0.03^{+0.03}_{-0.02}$	$3.2^{+1.1}_{-0.5}$	$1.2^{+0.8}_{-0.6}$	$0.12^{+0.18}_{-0.08}$	372 ± 112	< 150	> 2.5	> 8.2	P
3	8.005	-20.47	$0.15^{+0.04}_{-0.07}$	$9.8^{+2.9}_{-3.2}$	$2.0^{+1.7}_{-0.8}$	$0.25^{+0.21}_{-0.16}$	1022 ± 129	163 ± 62	6.3 ± 2.3	> 8.1	P
4	7.9932	-19.44	$0.33^{+0.12}_{-0.09}$	$16.3^{+21.0}_{-8.1}$	$8.7^{+6.3}_{-4.4}$	$0.10^{+0.18}_{-0.07}$	430 ± 69	< 166	> 2.6	\dots^{\dagger}	M
7	8.876	-20.75	$0.03^{+0.03}_{-0.02}$	$3.9^{+1.1}_{-0.6}$	$1.2^{+0.9}_{-0.6}$	$0.13^{+0.25}_{-0.09}$	895 ± 436	350 ± 194	2.6 ± 0.8	> 5.5	M
20	7.769	-18.55	$0.61^{+0.02}_{-0.18}$	$64.3^{+18.6}_{-50.8}$	$30.6^{+19.7}_{-13.0}$	$0.08^{+0.13}_{-0.06}$	109 ± 19	50 ± 16	2.2 ± 0.8	> 6.1	P
23	8.8805	-18.38	$0.06^{+0.1}_{-0.04}$	$0.8^{+0.7}_{-0.3}$	$0.2^{+0.2}_{-0.1}$	$0.21^{+0.23}_{-0.14}$	1195 ± 200	208 ± 121	5.8 ± 3.3	> 6.5	M
24	8.998	-19.08	$0.09^{+0.08}_{-0.06}$	$2.7^{+1.5}_{-1.0}$	$0.6^{+0.6}_{-0.3}$	$0.23^{+0.22}_{-0.15}$	989 ± 131	173 ± 51	5.7 ± 1.7	> 5.0	M

NOTE— (1) Source ID. (2) Spectroscopic redshift. (3) Absolute UV luminosity, calculated from the F150W filter. (4) Dust extinction. (5) Average SFR over 10 Myr. (6) Stellar mass. (7) Fraction of the mass contributed by the young (< 10 Myr) stellar population. (8) Rest-frame equivalent width of [O III]5008 line. (9) Rest-frame equivalent width of H β line. (10) [O III]5008/H β ratio. (11) [O III]5008/[O II]3727 ratio. (12) NIRSspec observation mode (P: prism, M: Medium Resolution). For the sources observed in both modes, we adopt the results with the better S/N in the brightest emission line. (4–7) values are estimated from the SED analysis with CIGALE, while (8–11) values are derived from the NIRSspec observations.

\dagger The [O II] line wavelength falls in the detector gap.

tinuum by correcting the slit-loss for the line emission (see Section 3.4) and subtracting the line contribution to the F444W photometry. We confirm that our EW measurements are consistent with the independent analysis and measurement for MPT-ID3, 23, and 24 presented in Tang et al. (2023) within the errors.

We do not detect [O II] with $S/N > 2$ from any of the z_{spec} sources. We thus place the conservative 3σ upper limits on the [O II] line and list the 3σ lower limits of O32 (\equiv [O III]5008/[O II]3727) in Table 2. We do not apply the slit-loss corrections for this calculation. Due to the wavelength dependence of the *JWST* point spread function, slit losses should be smaller for [O II] compared to [O III], and a slit loss correction would increase O32. Thus, the uncorrected lower limit for O32 is a conservative estimate.

Note that there are several other line features that show the peak pixel $S/N \sim 1 - 3$ at the expected wavelength positions (e.g., [Ne III], N V) in the 1D spectra, while in most of the cases, the y-axis position of the positive signals within the extracted aperture is not exactly matched with that of the brightest [O III]5008 line. Although we cannot rule out the possibility of the differential distribution of the emission lines⁴ or the effect of the noise fluctuation in these low S/N , we do not focus on the other emission lines in this paper.

3.4. Slitloss Correction

As mentioned in Section 2.3, we do not apply the default slitloss correction implemented in the calibration pipeline. Instead, we evaluate the scaling factor for the slit-loss correction in the two following approaches. In the first approach, we convolve and integrate the 1D spectrum with the filter response of F444W and obtain the scaling factor to match it with the total flux measured in the NIRCам/F444W photometry. In the second approach, we calculate the flux in the F444W map enclosed within the $0''.2 \times 0''.46$ shutter based on the source and MSA shutter positions and estimate the scaling factor to match it with the total flux measurement. We find that MPT-ID4 and ID7 show negative values in the first approach, indicating that integrated values are dominated by noise fluctuation even with the inclusion of the strong line emission in some faint sources. We thus adopt the second approach for MPT-ID4 and ID7, while we use the first for the rest of our targets. When we compare these two approaches using some bright targets, we find that the scaling factor can be different by ~ 10 –40%. This is likely caused by unknown offsets of targets within the MSA shutter related to the accuracy of the MSA alignment or the photometric calibrations between NIRCам and NIRSspec, which cannot be corrected in the second approach. An extended [O III]+H β structure has been identified around a lensed galaxy at $z = 8.5$ (Fujimoto et al. 2022b), and the differential spatial distribution between the ionized gas and the underlying continuum emission is also another unknown uncertainty in both approaches. We thus caution the readers that additional uncertainty might exist in the measurements due to the slit-loss correction steps.

⁴ For example, spatial offsets between the faint AGNs and the hosts have been reported in Ding et al. (2022), where highly ionized emission lines might be observed with spatial offsets.

3.5. SED Analysis

We analyze the physical properties of the seven spectroscopically confirmed NIRCcam galaxies using CIGALE. The details will be presented in Burgarella et al. (in prep.), and here we briefly explain our SED model. We include the *HST*+*JWST*/NIRCcam photometry as well as the $\text{EW}([\text{O III}]\lambda 5008)$ in the fit. We use the stellar synthesis population model of BPASS-v2 (Eldridge et al. 2017) with the lowest available $Z_{\text{BPASS}} = 0.0001$, where $Z_{\odot} = 0.014$. We assume a delayed+final burst (younger than 10 Myr) star-formation history (SFH) with the mass fraction from the recent burst activity of $f_{\text{burst}} = 0.03 - 0.5$. We adopt the dust attenuation law from Calzetti et al. (2000) for the stellar continuum and a screen model with an SMC extinction curve (Pei 1992) for the nebular emission (continuum + lines). During the SED fitting, we assume the $E(B - V)_{\text{stellar}} = 0.5 \times E(B - V)_{\text{line}}$. The results of SFR, M_{star} , and $E(B - V)$ are summarized in Table 2. Our NIRCcam-selected spec- z confirmed sources are generally characterized as $\text{SFR} \simeq 4 M_{\odot} \text{ yr}^{-1}$, $M_{\text{star}} \simeq 10^8 M_{\odot}$, $E(B - V) \simeq 0.1$, and $f_{\text{burst}} \simeq 20\%$.

Note that the SED analysis with the spatially-integrated photometry may systematically underestimate the stellar mass, especially in the strong emission line systems (Giménez-Arteaga et al. 2022; Papovich et al. 2022a). In our analysis, this effect is mitigated by constraining the f_{burst} factor in 0–50%, which provides the median of $f_{\text{burst}} \simeq 20\%$ in our sample. The $f_{\text{burst}} \simeq 20\%$ is well separated by the boundaries and consistent with recent results of the pixel-based spatially-resolved SED analysis for lensed galaxies at $z = 5 - 8.5$ with NIRCcam (Giménez-Arteaga et al. 2022). The consistency and potential differences among different SED models are further discussed in Burgarella et al. (in prep.).

4. RESULTS & DISCUSSIONS

4.1. Validity of High-redshift Galaxy Selection

In Figure 3, we present the M_{UV} -redshift relation among the z_{spec} confirmed and photometric sources. Among the 11 NIRCcam-selected high-redshift galaxy candidates, we confirm the spectroscopic redshifts of 7 galaxies at $z = 7.769 - 8.998$. Our CEERS observations demonstrate the capability of NIRSpec to determine the redshift even with a ~ 50 -min exposure down to $M_{\text{UV}} \simeq -18$ mag at $z \simeq 9$. On the other hand, the z_{spec} confirmation at $z \gtrsim 10$ in the UV bright regime ($M_{\text{UV}} \lesssim -20$ mag) has not yet been explored, likely due to the limited depth of our observations and the lack of strong emission lines observable at these higher redshifts within the NIRSpec wavelength coverage.

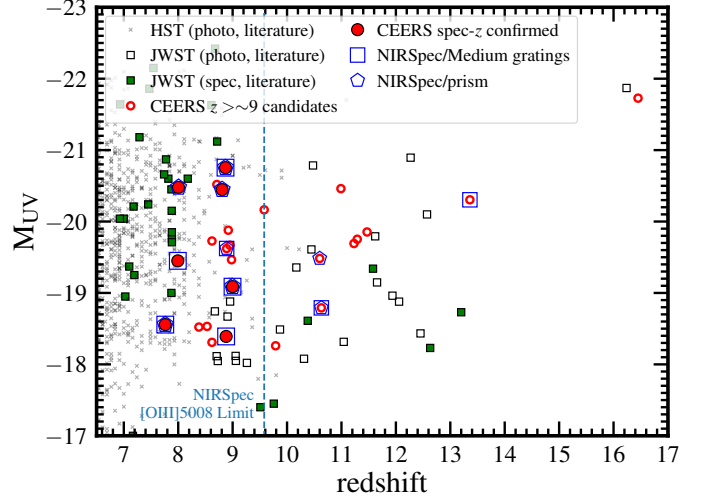


Figure 3. Status of spectroscopic confirmation at $z \gtrsim 8$ with *JWST*. The red open circles show the 26 candidates at $z \gtrsim 9$ in CEERS presented in (Finkelstein et al. 2022b), where the red filled circles indicate the sources spectroscopically confirmed in this study. The open blue pentagon and square indicate the observation mode of prism and Medium gratings, respectively. The green squares indicate other z_{spec} confirmed galaxies taken from recent *JWST* studies showing both M_{UV} and z_{spec} measurements, from lensing cluster fields (Williams et al. 2022; Roberts-Borsani et al. 2022; Mascia et al. 2023) and general fields (Tang et al. 2023; Curtis-Lake et al. 2022; Robertson et al. 2022). The dashed vertical line presents the redshift limitation to detect the $[\text{O III}]\lambda 5008$ line with NIRSpec.

If we examine the success ratio based on each redshift range according to the original z_{phot} estimates of our targets, we achieve the spectroscopic confirmation in six out of seven ($\simeq 90\%$) targets with $8.8 \lesssim z_{\text{phot}} \lesssim 9.5$. Owing to the homogeneous sample selection and sensitivity in the follow-up spectroscopy, our results indicate that the classical z_{phot} technique assures at least $\sim 90\%$ of the high-redshift galaxy selection. This is helpful to interpret the recent and future UVLF results out to $z \sim 9$ that are also measured via similar dropout or z_{phot} techniques with NIRCcam (e.g., Donnan et al. 2022b; Harikane et al. 2022; Bouwens et al. 2022b,a). Importantly, CEERS does not include a NIRCcam-based dropout filter for the $z \simeq 9$ galaxy selection (e.g., F090W), and instead, it relies on the *HST*/ACS F814W filter with a 5σ limiting AB magnitude for a point source of 28.3 mag (Finkelstein et al. 2022b). Therefore reliable

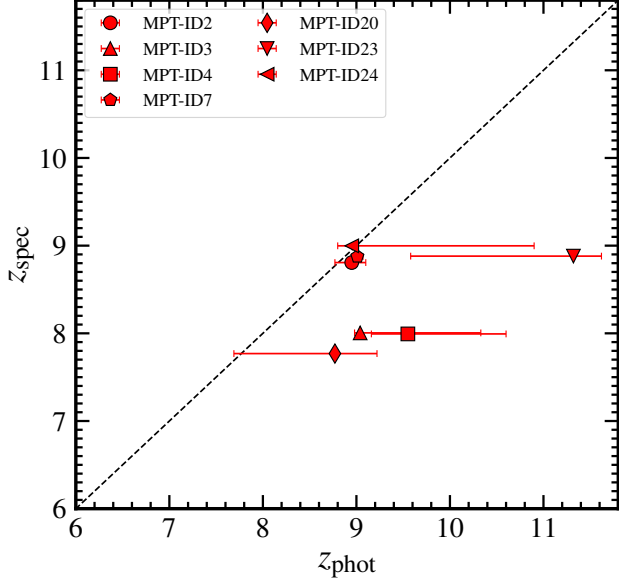


Figure 4. Photometric vs. spectroscopic redshift for the NIRCam-selected galaxies with $z_{\text{phot}} \gtrsim 9$. Six out of seven sources show $z_{\text{spec}} < z_{\text{phot}}$, though all are consistent within 2σ .

high-redshift galaxy selection could be further improved by the addition of a deeper NIRCam dropout filter⁵.

Interestingly, the majority of our z_{spec} sample has a z_{spec} value smaller than the $P(z)$ peak. In Figure 4, we compare the z_{phot} and z_{spec} values for our z_{spec} sample. Although all z_{spec} values fall within the 2σ range of $P(z)$ (see Figure 2), three out of seven sources show $z_{\text{spec}} < z_{\text{phot}}$ beyond the 1σ uncertainty. The z_{phot} value and the entire $P(z)$ shape largely depend on the galaxy models used in the SED fitting. In our original target selection (Section 2.1), the high-redshift galaxy candidates are selected by using the SED fitting code EAZY (Brammer et al. 2008) based on the FSPS-based (Conroy & Gunn 2010) default 12 template sets in EAZY and 6 additional templates presented in Larson et al. (2022). These six additional templates are created by combining stellar population spectra from BPASS (Eldridge & Stanway 2009) and CLOUDY (Ferland et al. 2017) to recover the rest-frame UV blue color space of young galaxies, which significantly recovers the color space of simulated early galaxies in a semi-analytic galaxy model (Yung et al. 2022). However, the high fraction of $z_{\text{spec}} < z_{\text{phot}}$ observed in our sample might indicate that the SED templates generally used in the high-redshift galaxy studies

are still insufficient to recover the rest-frame UV color space of $z \gtrsim 8$ galaxies, or that the modeling of the IGM is incomplete in some way (though likely *not* due to the damping wing effect discussed in Curtis-Lake et al. 2022, which would lead to redshift differences much smaller than we observe here). This could also show the possible limitations inherent in using a single photo- z code (e.g., Dahlen et al. 2013). Another reason might be the difficulty of determining the redshift at $z \gtrsim 9.5$ due to the lack of strong emission lines in the NIRSpec wavelength coverage. Then, while the true redshifts are distributed on both sides of the peak of $P(z)$ according to uncertainties in the broadband photometry, the spec- z confirmation may be biased to $z \lesssim 9.5$ when the sensitivity is not deep enough to capture the Lyman- α break (Curtis-Lake et al. 2022; Robertson et al. 2022; Roberts-Borsani et al. 2022) and has to rely on the line identification to determine z_{spec} . The absence of the NIRCam-based dropout filter may also at least partially contribute to the $>1\sigma$ difference between z_{phot} and z_{spec} for these sources.

Of the other four targets with $z_{\text{phot}} > 10$, one target turns out to be $z_{\text{spec}} = 8.8802$ (MPT-ID 23), while no robust lines are identified in the other three targets. The lack of lines might be because [O III]+H β is redshifted beyond the NIRSpec wavelength range at $z \gtrsim 10$. Given that one out of four has been confirmed at $z_{\text{spec}} < 10$, this would imply that 75% ($=3/4$) candidates might be truly at $z > 10$. Once the success rate of the high-redshift galaxy selection is also confirmed at $z_{\text{phot}} \gtrsim 10$, again, it will be widely useful to interpret the photometric-based UVLF measurements, which are now explored out to $z \sim 17$ with NIRCam (e.g., Harikane et al. 2022; Donnan et al. 2022b,a; Bouwens et al. 2022b,a; Finkelstein et al. 2022b). This will enable us to verify the recent arguments of the high abundance of bright galaxies at these early epochs of the universe, which may challenge the current galaxy formation and evolution models.

4.2. Properties of Galaxies at $z = 8-9$

The high z_{spec} confirmation rate ($\simeq 90\%$) for the $z_{\text{phot}} \sim 9$ targets from the homogeneous LBG selection indicates that our spec- z sample is representative of the majority of the NIRCam-selected LBG population at $z = 8-9$. Moreover, recent UVLF studies suggest that the characteristic UV luminosity is $M_{\text{UV}}^* \sim -21$ mag in the Schechter function form (e.g., Finkelstein et al. 2015; Bouwens et al. 2021; Harikane et al. 2022). Therefore, our NIRCam-selected z_{spec} sources, ranging in the UV luminosity of $M_{\text{UV}} \in [-21, -18]$, are sub- L^* populations down to $\simeq 0.001 \times L^*$, which is helpful to understand the typical physical properties of the abundant faint popula-

⁵ For example, the GLASS-JWST (Treu et al. 2022) survey includes the F090W filter, where robust $z = 11-13$ candidates have been reported (e.g., Castellano et al. 2022; Naidu et al. 2022a).

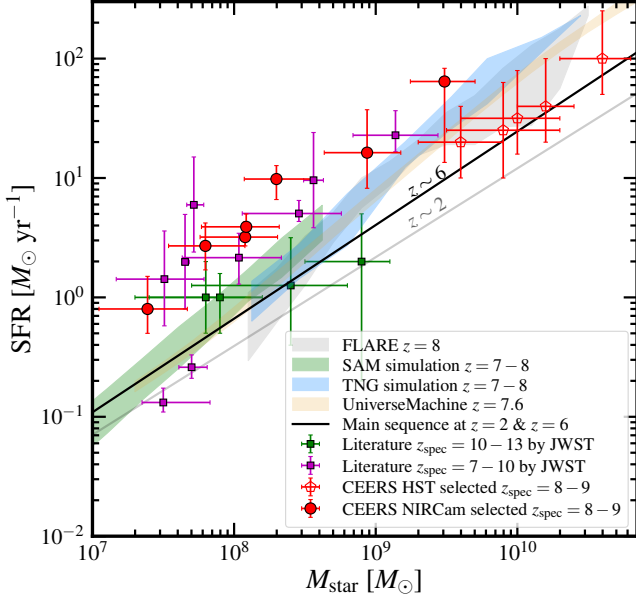


Figure 5. SFR vs. M_{star} . The filled and open symbols represent the spec- z and photometric samples, respectively. The filled red circles show our z_{spec} sample. The magenta and green squares are recent *JWST* results for lensed galaxies at $z \sim 7 - 10$ (Tacchella et al. 2022a; Williams et al. 2022; Roberts-Borsani et al. 2022; Heintz et al. 2022a) and for general field galaxies at $z \sim 10 - 13$ (Robertson et al. 2022; Curtis-Lake et al. 2022), respectively. The red pentagons show recent *HST*+IRAC results for bright galaxies at $z \sim 8 - 9$ in the EGS field (Tacchella et al. 2022b). The black and grey lines denote the best-fit relations at $z = 2$ and $z = 6$ (Iyer et al. 2018). The color-shaded regions present the 16-84th percentile of simulated galaxies (Yung et al. 2019b, 2022; Behroozi et al. 2019, 2020; Wilkins et al. 2022b,a). Our NIRCAM-selected galaxies at $z_{\text{spec}} = 8 - 9$ show high sSFR ($\simeq 40 \text{ Gyr}^{-1}$) compared to the $z = 2 - 6$ main sequence.

tion without gravitational lensing uncertainties. In the following subsections, we thus carry out the first census of the physical properties of spectroscopically-confirmed sub- L^* galaxies at this redshift range and investigate the potential difference from bright galaxies ($M_{\text{UV}} \simeq -22$) identified in previous *HST* studies and also spectroscopically confirmed at similar redshifts (Larson et al., in prep.).

4.2.1. SFR vs. M_{star}

Figure 5 presents the SFR- M_{star} relation. For comparison, we show the main sequence estimated at $z = 2$ and $z = 6$ (Iyer et al. 2018), recent *JWST* results for the sources spectroscopically confirmed at $z = 7 - 13$ (Tacchella et al. 2022a; Williams et al. 2022; Roberts-Borsani et al. 2022; Heintz et al. 2022a; Robertson et al. 2022; Curtis-Lake et al. 2022), recent *HST*+IRAC results for bright galaxies at $z_{\text{phot}} \sim 8 - 9$ (Tacchella et al.

2022b), and the 16-84th percentile of the distribution of simulated galaxies at $z = 7 - 8$ (Yung et al. 2019b, 2022; Behroozi et al. 2019, 2020; Nelson et al. 2019; Wilkins et al. 2022b,a). Note that we use the SED-based SFR estimate (Section 3.5), instead of using the $H\beta$ line. This is because of the potential uncertainty in the slit-loss correction (Section 3.4). Also, an extended $[\text{O III}]+H\beta$ structure has been recently reported around a lensed galaxy at $z = 8.5$, which might make the $H\beta$ -based SFR measurement to be overestimated by counting the $H\beta$ emission caused by other physical mechanisms such as powerful outflows (Fujimoto et al. 2022b).

In Figure 5, we find that our NIRCAM-selected sample (red filled circles) has a SFR- M_{star} relation generally consistent with the recent *JWST* results for lensed galaxies at $z = 7 - 10$ (magenta squares) down to $\sim 7 \times 10^7 M_{\odot}$, which is less star-forming and less massive than the *HST*-selected bright galaxies at similar redshifts (red open pentagons) down to a ~ 1.5 -dex scale. We also find that most of our z_{spec} sample and the lensed galaxies in the literature fall above the $z = 6$ main sequence by a ~ 0.5 -dex scale beyond the errors at a given M_{star} , showing a relatively high specific SFR (sSFR $\equiv \text{SFR}/M_{\text{star}}$) of $\simeq 40 \text{ Gyr}^{-1}$. This is consistent with recent *JWST* results that less luminous LBGs at $z \sim 7 - 8$ have similarly high sSFR of $\simeq 80 \text{ Gyr}^{-1}$ from a photometric, but more statistical ($N = 118$) sample (Endsley et al. 2022). As discussed in Endsley et al. (2022), the high sSFR in the less luminous LBGs, highlighted by our z_{spec} sample and the lensed galaxies, is likely caused by young stellar populations. This is consistent with our SED results showing the presence of the young stellar populations ($< 10 \text{ Myrs}$) accounting for the total mass of $\simeq 20\%$ of the galaxy mass (Table 2). The increasing sSFR trend as a function of redshift has been observed at lower redshifts (e.g., Speagle et al. 2014; Tasca et al. 2015; Khusanova et al. 2020). Our results may indicate that this increasing trend continues at least out to $z = 8 - 9$. We also confirm the general agreement with predictions from the simulations within the errors.

Note that a different SFH assumption may impact our SED estimates. For example, our parametric (delayed + final burst $< 10 \text{ Myr}$) approach might miss an extended tail of older star-forming activity in the SFH. However, we confirm that the mass estimate increases by a factor of ~ 2 at most in our sample by using the Dense Basis (Iyer et al. 2019) fitting code with a non-parametric SFH assumption, which is still insufficient to match the distribution with the main sequence at $z = 2 - 6$. The general agreement with measurements from a variety of literature sources for lensed galaxies also suggests that the impact from different SFH assumptions and SED

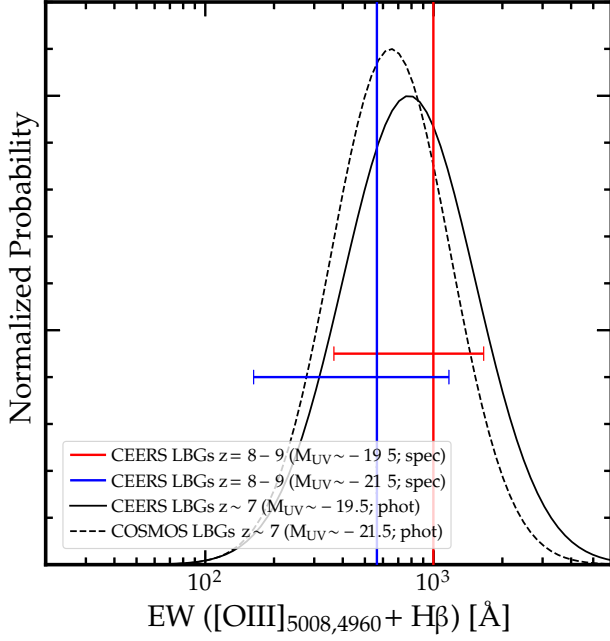


Figure 6. Rest-frame EW distribution of $[\text{O III}]+\text{H}\beta$. The red and blue lines and error bars present the median and 16–84th percentiles of fainter (NIRCam-selected) and brighter (*HST*-selected, Larson et al., in prep.) LBGs with spectroscopic redshifts $z = 8 - 9$. The black solid and dashed curves show the best-fit log-normal distribution estimated from SED analysis for photometric samples of 36 luminous LBGs at $z \simeq 6.6 - 6.9$ identified in the COSMOS field ($M_{\text{UV}} \sim 21.5$ mag) and 118 less luminous LBGs at $z \sim 6.5 - 8$ in CEERS (Endsley et al. 2022).

modelings is likely small. It should also be noted that the slight excess of the observational results compared to the distribution of the simulated galaxies at $z = 7 - 8$ might be caused by the observation bias, which is not counted in the simulated galaxies due to the difficulty of quantifying the spec- z confirmation process in the observation. However, the main sequence at $z = 2 - 6$ is also measured by observations that should include a similar bias. Therefore, the relatively high sSFR of the $z = 8 - 9$ galaxies, compared to that of the $z = 2 - 6$ galaxies, is unlikely explained by the observation bias.

4.2.2. $[\text{O III}]+\text{H}\beta$ EW

In the previous subsections, the sSFR values determined for our z_{spec} sources are higher than those for $z \sim 6$ main-sequence galaxies, which is likely because of the young stellar populations at higher redshifts. From photometric-based SED analysis, high $\text{EW}([\text{O III}]+\text{H}\beta)$ values ($> 1000\text{\AA}$) have been observed in galaxies at $z \simeq 6 - 9$ in previous *HST*+IRAC studies (e.g., Labbé et al. 2013; De Barros et al. 2019; Endsley et al. 2021), where the high $\text{EW}([\text{O III}]+\text{H}\beta)$ are thought to be caused by

the light from very young (1–10 Myr) stellar populations (e.g., Amorín et al. 2017; Tang et al. 2019; Vanzella et al. 2020). To have an independent insight into the stellar population and ISM properties of our galaxies, we thus compare the $\text{EW}([\text{O III}]+\text{H}\beta)$ values of our NIRCam-selected galaxies with other galaxy populations in this subsection.

In Figure 6, we show the median (red line) and 16–84th percentile (red bar) of the rest-frame $[\text{O III}]+\text{H}\beta$ EW measurement for our z_{spec} sample. In the same manner, we also measure and show the median and 16–84th percentile of $[\text{O III}]+\text{H}\beta$ EW values for a sample of brighter *HST*-selected LBGs in CEERS (blue line and bar), also spectroscopically confirmed at $z = 8 - 9$ (Larson et al., in prep). The 16–84th percentile is estimated by assuming the log-normal probability distribution for the EW measurements of each source and summing them to define the entire probability distribution. The upper limits of $\text{H}\beta$ EW (MPT-ID2, 4) are also included in this calculation, assuming that zero and the 3σ error correspond to its center and standard deviation of the log-normal distribution. For comparison, we also present the EW distribution estimated from the photometric-based SED analysis for LBGs at $z \sim 7$ with similar UV luminosity ($M_{\text{UV}} \sim -19.5$; solid line) with *JWST* data and brighter LBGs ($M_{\text{UV}} \sim -21.5$; dashed line) at $z \sim 7$ (Endsley et al. 2022).

We obtain median $\text{EW}([\text{O III}]+\text{H}\beta)$ values of $1100^{+560}_{-730}\text{\AA}$ and $570^{+590}_{-410}\text{\AA}$ for the spec- z confirmed, NIRCam-selected and *HST*-selected luminous galaxies, respectively. These measurements are generally much higher than $z = 1 - 4$ galaxies with similar SFR ($\simeq 100 - 200\text{\AA}$; Reddy et al. 2018), but consistent with the previous photometric-based measurements for $z = 7 - 8$ galaxies ($\simeq 600 - 800\text{\AA}$; Labbé et al. e.g., 2013; De Barros et al. e.g., 2019; Endsley et al. e.g., 2021). We find that less luminous galaxies have higher $\text{EW}([\text{O III}]+\text{H}\beta)$ values, while the difference is still consistent within the 1σ ranges. The slight increase of $\text{EW}([\text{O III}]+\text{H}\beta)$ in less luminous galaxies agrees with the trend observed in the recent photometric-based results (solid and dashed curves). The increasing trend of $\text{EW}([\text{O III}]+\text{H}\beta)$ with decreasing metallicity has been observed at $z = 1 - 4$ (Reddy et al. 2018). However, in extremely metal-poor systems, the $[\text{O III}]$ emission should be suppressed due to the low oxygen abundance, and the $\text{EW}([\text{O III}]+\text{H}\beta)$ value significantly decreases at a given ionizing photons. Therefore, the slight increase of $\text{EW}([\text{O III}]+\text{H}\beta)$ observed in our NIRCam-selected galaxies at $z = 8 - 9$ would indicate that these less luminous galaxies are more metal-poor systems than the luminous galaxies, but not extremely metal-poor

systems. The high $\text{EW}([\text{O III}]+\text{H}\beta)$ value might also be supported by more ionizing photon inputs. Recent studies report the detection of the intense nebular emission from highly ionized carbon in the rest-frame UV from $z > 7$ galaxies (Stark et al. 2015, 2017; Laporte et al. 2017; Mainali et al. 2018; Schmidt et al. 2017; Hutchison et al. 2019). From a deep IRAC $5.8\mu\text{m}$ band stacking for $z \sim 8$ LBGs, Stefanon et al. (2022) report a large $\text{H}\alpha+[\text{N II}]$ EW and subsequently derive a very high ionizing photon production efficiency of $\log(\xi_{\text{ion}}/\text{Hz erg}^{-1}) = 25.97^{+0.18}_{-0.28}$. The redshift evolution of the electron density has also been reported, reaching $n_e \gtrsim 300 \text{ cm}^{-3}$ at $z \sim 9$ (Isobe et al. 2023). These results suggest that higher redshift, younger galaxies have a higher ionized ISM condition than lower- z galaxies, which may lead to maintaining the high $\text{EW}([\text{O III}]+\text{H}\beta)$ distribution even in our NIRCcam-selected less luminous galaxies at $z = 8 - 9$. We caution that our results might be biased toward the high EW systems, given the fact that the spec- z of high EW systems is easily confirmed via bright emission lines, although our z_{spec} sample represents $\simeq 90\%$ of the less luminous LBGs at $z \sim 8 - 9$ from the homogeneous selection (Section 4.1). The presence or absence of the increasing trend of $\text{EW}([\text{O III}]+\text{H}\beta)$ distribution as a function of UV luminosity and redshift will be further investigated with larger spectroscopic samples in a separate paper.

4.2.3. Ionizing photon production efficiency

To place our z_{spec} sample in the context of cosmic reionization, we also estimate the production efficiency of ionizing photons, ξ_{ion} . We measure the ξ_{ion} values via the Balmer recombination line approach (e.g., Bouwens et al. 2016) based on the $\text{H}\beta$ line in the same manner as Matthee et al. (2022a) by assuming a zero escape fraction of ionizing photons. A correction for dust attenuation is applied based on our SED fitting results (Section 3.5). For comparison, we measure ξ_{ion} also for the z_{spec} confirmed *HST*-selected, luminous LBGs (Larson et al., in prep.) in the same manner.

In Figure 7, we show our ξ_{ion} estimates with recent spectroscopic results in different galaxy populations at high redshifts (Stark et al. 2015, 2017; Matthee et al. 2017, 2022a; Atek et al. 2022; Naidu et al. 2022a; Tang et al. 2019; Maseda et al. 2020) and the canonical value that has been used when modeling the contributions of galaxies to the cosmic reionization (e.g., Robertson et al. 2013). To perform a statistical comparison, we present the median and 16-84th percentile as the error bar for our ξ_{ion} estimates of our z_{spec} sample by assuming a log-normal probability distribution for the ξ_{ion} measurement of each source. Upper limits for $\text{H}\beta$

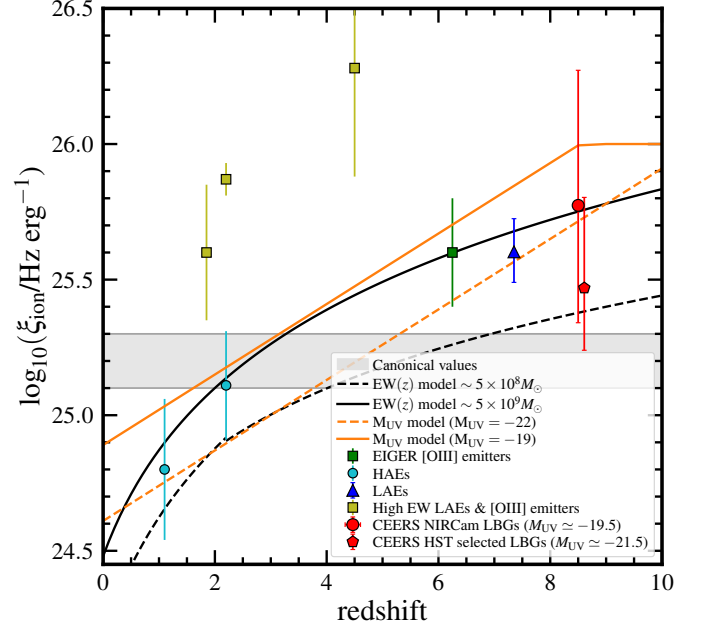


Figure 7. Redshift evolution of the ionizing photon production efficiency ξ_{ion} . The red-filled circle and pentagon with error bars present the median and 16-84th percentiles of the spec- z confirmed, less luminous and luminous LBGs at $z = 8 - 9$ selected by NIRCcam and *HST* (Larson et al. in prep.), respectively. Other color symbols are taken or calculated from the literature based on spectroscopy, showing the median/average values for a variety of populations: $[\text{O III}]$ emitters at $z \sim 6$ (green squares: Matthee et al. 2022a), Lyman α emitters at $z \sim 7$ (LAEs, blue triangle; Stark et al. 2015, 2017), $\text{H}\alpha$ emitters at $z \sim 1 - 2$ (HAEs, cyan circles; Matthee et al. 2017; Atek et al. 2022), and LAEs and $[\text{O III}]$ emitters with high EWs (deep yellow squares; Tang et al. 2019; Maseda et al. 2020; Naidu et al. 2022a). The grey shade shows the canonical value (e.g., Robertson et al. 2013), and the dashed and solid curves are predictions from empirical models based on $\text{H}\alpha$ EW (black curves; Faisst et al. 2016; Matthee et al. 2017) and UV luminosity (orange curve; Finkelstein et al. 2019).

line fluxes (MPT-ID2, 4) are also included by assuming that the canonical value and ± 0.1 correspond to its center and standard deviation of the log-normal distribution, respectively. We obtain $\log(\xi_{\text{ion}}/\text{Hz erg}^{-1}) = 25.77^{+0.50}_{-0.43}$ and $25.47^{+0.33}_{-0.23}$ for the NIRCcam- and *HST*-selected sources, respectively. We find that these median ξ_{ion} values in our sample are much higher than the measurements at $z \sim 1-2$ and the canonical value, but consistent with the recent result for the $[\text{O III}]$ emitters (green square) and Lyman- α emitters (blue triangle) at $z \sim 6 - 7$, and the strong line-emitting galaxies at $z \sim 2 - 4$ (yellow squares). Our results are also consistent with the deep IRAC $5.8\mu\text{m}$ band stacking results for $z \sim 8$ LBGs ($25.97^{+0.18}_{-0.28}$; Stefanon et al. 2022). We

also find that less luminous, NIRCam-selected galaxies have higher ξ_{ion} than that of *HST*-selected galaxies. Although these two measurements are consistent within the 1σ ranges, this trend is also along the empirical redshift evolution models for the increasing ξ_{ion} at fixed mass (Faisst et al. 2016; Matthee et al. 2017) and UV luminosity (Finkelstein et al. 2019), suggesting the key contributions of faint galaxies to cosmic reionization.

As discussed in previous studies (e.g., Finkelstein et al. 2019; Stefanon et al. 2022; Matthee et al. 2022a), the ξ_{ion} estimates higher than the canonical values require the modest ($\ll 20\%$) escape fractions of ionizing photons (e.g., Davies et al. 2021) or that the contribution from faint galaxies ($M_{\text{UV}} > -17$; e.g., Matthee et al. 2022b) is minor. Albeit the small statistics, our z_{spec} sample represents the majority ($\simeq 90\%$) of the LBGs at $z = 8 - 9$ (Section 4.1), which may support the arguments of the modest escape fraction or the negligible contribution from further faint galaxies. However, the high ξ_{ion} measurements observed in galaxies $z \gtrsim 6$ are challenging to the current physics-based galaxy formation models (e.g., Wilkins et al. 2016; Yung et al. 2020b) with standard model components (e.g., power-law IMFs and simple stellar population SEDs). A top-heavy IMF and metal-free star SED in galaxies at these epochs are potential explanations to account for this discrepancy (e.g., Zackrisson et al. 2011; Trussler et al. 2022). Together with the faint-end measurements of the UVLFs at $z > 8$, the contribution of the faint LBG populations to the cosmic reionization, and relevant physical mechanisms, will also be further investigated in separate papers.

4.2.4. Chemical Evolution

The rest-frame optical emission lines have been the most intensively calibrated and widely exploited to constrain the metallicity in distant galaxies in the limitation of high-redshift observations (see review e.g., Maiolino & Mannucci 2019). Our NIRSpect observations cover the wavelength of the key optical emission lines of [O III]5008, $\text{H}\beta$, and [O II]3727. However, we do not securely detect any [O II] lines from our z_{spec} sample. We thus focus on the R3 ([O III]/ $\text{H}\beta$) measurement to examine the oxygen abundance in the following analysis, assuming a negligible contribution from [O II]. The general agreement in the metallicity measurement between the R3-based method and the direct electron temperature method has been confirmed even at $z = 5 - 8$ galaxies in recent *JWST* studies based on the successful aural [O III]4363 line detection (e.g., Curti et al. 2022; Matthee et al. 2022a).

In the left panel of Figure 8, we show our R3 measurements as a function of M_{star} . We also measure and show the *HST*-selected, luminous LBGs (Larson et al., in prep.) in the same manner, while we take their M_{star} estimates from Tacchella et al. (2022b). These NIRCam- and *HST*-selected samples enlarge the M_{star} parameter space and provide a unique opportunity to examine the mass-metallicity relation in a fair manner, owing to the homogeneous sample selection and follow-up sensitivity. For comparison, we also present the recent results for field galaxies at $z = 2 - 3$ (Sanders et al. 2020; Papovich et al. 2022a) and $z = 5 - 7$ (Matthee et al. 2022a) and lensed galaxies at $z = 7.5 - 9.5$ (Trump et al. 2022; Williams et al. 2022; Heintz et al. 2022b; Mascia et al. 2023). By implication, the R3- M_{star} relation at $z = 2$ is extrapolated by converting the $z = 2$ mass-metallicity relation (Sanders et al. 2020) based on the R3-metallicity calibration presented in Nakajima et al. (2022). We also show predictions from cosmological galaxy evolution models, incorporating the nebular emission line (Nelson et al. 2019; Yung et al. 2019b, 2022; Hirschmann et al. 2022; Wilkins et al. 2022b,a).

First, we find in our NIRCam- and *HST*-selected samples that there is an increasing trend in R3 with increasing M_{star} . This trend is different from the results at $z \sim 2 - 3$ (black squares) but generally consistent with the model predictions (color-shaded regions), where the increasing trend is explained by the high ionization parameter in early galaxies (Hirschmann et al. 2022; Hirschmann et al., in prep.). High O32 values of $\gtrsim 10$ have been reported from the composite spectrum for $z \sim 7.5$ galaxies (Sanders et al. 2023; Tang et al. 2023), which also suggests the highly ionized ISM state in early galaxies. Second, we compare our measurements with recent *JWST* results and find that our NIRCam-selected galaxies show the R3- M_{star} distribution similar to the lensed galaxies at $z = 7.5 - 9.5$, ranging over the R3 values of $\sim 2 - 6$ that are generally comparable or lower than those of the field galaxies at $z = 5 - 7$. Below $12 + \log(O/H) \approx 8$, the R3 values generally decrease towards low metallicity because the [O III] emission is suppressed in the low oxygen abundance (e.g., Maiolino et al. 2008; Curti et al. 2017; Bian et al. 2018; Nakajima et al. 2022). Thus, the lower R3 values in our and lensed galaxies at $z \gtrsim 8$ with respect to the $z = 5 - 7$ field galaxies might indicate a decreasing trend of metallicity at a given M_{star} towards high redshifts. Although a few sources are placed much below the other sources and the model predictions at $\log(M_{\text{star}}/M_{\odot}) \gtrsim 8.5$, this might indicate that the pristine gas inflow might be taking place in these exceptional galaxies, which maintains

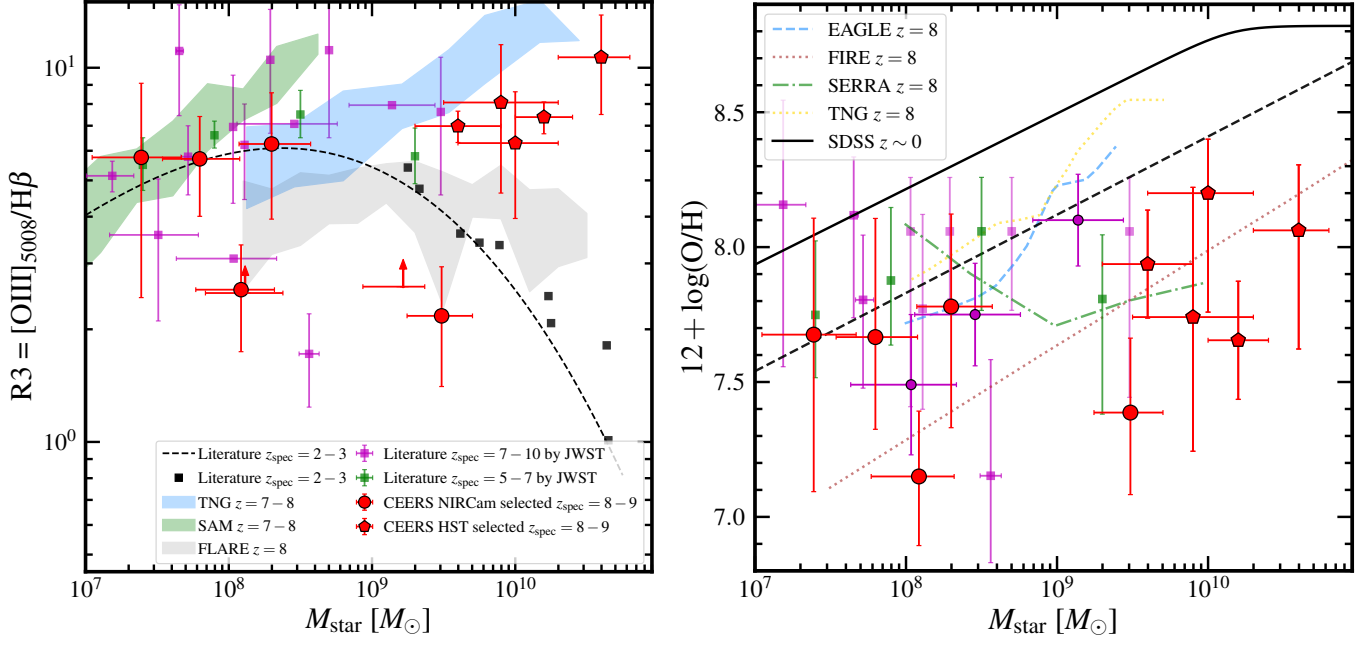


Figure 8. **Left:** $R3$ vs. M_{star} relation. The red circles and pentagons present our NIRCam- and *HST*-selected galaxies at $z = 8 - 9$ in CEERS, respectively, including lower limits. The magenta and green squares denote the recent *JWST* results for lensed galaxies at $z = 7.5 - 9.5$ (Trump et al. 2022; Williams et al. 2022; Heintz et al. 2022c; Mascia et al. 2023) and general field galaxies at $z = 5 - 7$ (Matthee et al. 2022a). The black squares show the results for general field galaxies at $z \sim 2 - 3$ (Sanders et al. 2020; Papovich et al. 2022a), where its $R3$ - M_{star} relation is extrapolated by converting the mass-metallicity relation based on the $R3$ calibration of Nakajima et al. (2022). The color-shaded indicate the 16-84th percentile of simulated galaxies at $z = 7 - 8$ in TNG50 and TNG100 (e.g., Nelson et al. 2019) and Santa Cruz SAM (e.g., Yung et al. 2019b, 2022), incorporating the nebular emission line calculations (Hirschmann et al. 2022), and FLARE (Wilkins et al. 2022b,a). **Right:** Metallicity vs. M_{star} relation. Our and other $R3$ measurements at $z > 7$ in the left panel are all converted based on the $R3$ -metallicity calibration (see text). The black lines are the best-fit relation at $z = 0$ (solid) and $z = 3$ (dashed) (Sanders et al. 2021), while the other color lines denote the predictions from simulations (Schaye et al. 2015; Ma et al. 2016; Pallottini et al. 2022; Ucci et al. 2023). The magenta circles are the measurements based on the $[\text{O III}]4363$ line for three lensed galaxies at $z = 7.7 - 8.5$ (e.g., Trump et al. 2022; Curti et al. 2022; Schaerer et al. 2022). The mass-metallicity relation at $z = 8 - 9$ is likely placed below the relations at $z = 0 - 3$, which is generally consistent with the predictions from simulations.

the oxygen abundance low and makes their $[\text{O III}]$ line emissivity very low.

In the right panel of Figure 8, we present the metallicity measurements at $z = 0 - 9$. We estimate the metallicities of our sample using the $R3$ calibration of Nakajima et al. (2022) that takes $\text{H}\beta$ EW (\approx ionization state) into account and expands the calibration down to $12 + \log(\text{O}/\text{H}) \simeq 6.9$ by analyzing the local extremely metal-poor galaxies. We obtain $12 + \log(\text{O}/\text{H}) \simeq 7.2 - 7.6$ for the NIRCam-selected galaxies at $z = 8 - 9$.⁶

⁶ For the sources with $\text{EW}(\text{H}\beta) > 150\text{\AA}$ and the other, we use the $R3$ -metallicity conversion calibrated for high ($\gtrsim 200\text{\AA}$) and low ($\lesssim 100\text{\AA}$) $\text{H}\beta$ EW sources in Nakajima et al. (2022), respectively. In this conversion, we assume that our NIRCam-selected sample has $12 + \log(\text{O}/\text{H}) \leq 8.2$, because of their less massive properties ($\lesssim 10^9 M_{\odot}$, see Figure 5) and lower limit of O32 (Table 2) that correspond to a low oxygen abundance of $12 + \log(\text{O}/\text{H}) \lesssim 8.2$ based on the O32 calibration (e.g., Maiolino et al. 2008; Curti et al. 2017; Bian et al. 2018; Pérez-Montero et al. 2021; Nakajima et al. 2022; Papovich et al. 2022b).

For the *HST*-selected galaxies, the high $R3$ values exceed the possible range in the calibration above, and we thus use another calibration for simulated galaxies at $z = 4 - 8$ (Hirschmann et al. 2022; Hirschmann et al., in prep.) that reproduces the increasing $R3$ trend with increasing M_{star} in the left panel. This yields $12 + \log(\text{O}/\text{H}) \simeq 7.6 - 8.2$ for the *HST*-selected galaxies. Based on these calibrations, we find that the galaxies at $z = 8 - 9$ fall below the mass metallicity relations at $z = 0 - 3$ (e.g., Sanders et al. 2021) extrapolated down to $M_{\text{star}} \sim 10^7 M_{\odot}$. This is generally consistent with the model predictions (e.g., Schaye et al. 2015; Ma et al. 2016; Pallottini et al. 2022; Ucci et al. 2023) and the recent *JWST* results of the mass-metallicity measurements at $z = 5 - 9.5$ (Matthee et al. 2022a; Heintz et al. 2022a), but with different calibrations (e.g., Bian et al. 2018; Curti et al. 2020). By applying the same $R3$ calibrations to these recent *JWST* results, we obtain $12 + \log(\text{O}/\text{H}) \simeq 7.7 - 8.1$ and $\simeq 7.2 - 8.2$ for

the $z = 5 - 7$ field galaxies and the lensed galaxies at $z = 7.5 - 9.5$, respectively. This implies that the metallicity of our NIRCcam-selected galaxies at $z = 8 - 9$ is consistent with the lensed galaxies at similar redshifts within the large scatter, but may be slightly lower than the field galaxies at $z = 5 - 7$. Combined with our SFR- M_{star} results (Section 4.2.1), we find that galaxies at $\log(M_{\text{star}}/M_{\odot}) \simeq 8 - 9$ have a trend of an increasing SFR and decreasing metallicity from $z \sim 2 - 6$ to $z \sim 8 - 9$.

5. SUMMARY

In this paper, we present *JWST* NIRSpec multi-object spectroscopy results for 11 high-redshift galaxy candidates at $z \simeq 9 - 13$ selected from deep NIRCcam data taken in June 2022 in the Cosmic Evolution Early Release Science (CEERS) field. All targets are observed with the prism or medium-resolution G140M/F100LP, G235M/F170LP and G395M/F290LP gratings, both of which continuously cover $\sim 1 - 5 \mu\text{m}$ wavelengths in the observed frame, maximizing the chance of spectroscopic confirmation either by emission lines or the Lyman- α break. This is the first homogeneous, luminosity-selected follow-up *JWST* spectroscopy for high-redshift galaxy candidates selected with NIRCcam in the UV luminosity range of $M_{\text{UV}} \in [-21, -18]$, setting the benchmark for future high-redshift galaxy selection at $z \gtrsim 9$ with NIRCcam. Comparing with the *HST*-selected luminous ($M_{\text{UV}} \simeq -22$) galaxies that are also spectroscopically confirmed at similar redshifts (Larson et al., in prep.), we also investigate the characteristics of these NIRCcam-selected galaxies. The main findings of this paper are summarized as follows:

1. We systematically analyze 1D and 2D spectra and spectroscopically confirm 7 out of 11 targets with [O III]5008, 4960 lines at $z = 7.762 - 8.998$. One of the candidates shows a potential single line detection at $5.20 \mu\text{m}$, which may indicate the galaxy redshift at $z = 9.386$ or $z = 9.697$, depending on whether the line is [O III]5008 or $\text{H}\beta$. We do not detect emission lines or Lyman- α continuum breaks in the other three candidates.
2. Based on the original z_{phot} estimate, the success ratio of the spec- z confirmation for $z_{\text{phot}} \sim 9$ candidates reaches $\simeq 90\%$ ($= 6/7$). No robust multiple-line identifications in three out of four $z_{\text{phot}} > 10$ candidates might indicate that strong optical emission lines (e.g., [O III]5008, $\text{H}\beta$) in these galaxies are redshifted beyond the NIRSpec wavelength range, and may support a high purity also in the $z_{\text{phot}} > 10$ candidate selection.

The spec- z confirmation results from the homogeneous sample selection and follow-up observations are widely useful to interpret the UV luminosity function studies now explored out to $z \sim 17$ with *JWST*/NIRCcam.

3. Although all z_{spec} values fall within the 2σ uncertainty of the original z_{phot} estimates, we find the majority of the sources show $z_{\text{spec}} < z_{\text{phot}}$, where almost half exceed the 1σ uncertainty. This may indicate that the galaxy templates generally used for high-redshift galaxy selection at $z \gtrsim 8$ are still insufficient to recover their rest-frame UV color space. This could also be caused by the possible limitations inherent in using a single photo- z code, the lack of a deep NIRCcam dropout filter (e.g., F090W), or the potential bias due to the fact that the strong line identification is limited out to $z \sim 9.5$.
4. We perform the SED fitting to the *HST*+NIRCcam photometry and [O III]5008 equivalent with (EW) and evaluate the star-formation rate (SFR) and stellar mass (M_{star}) relation for the seven spec- z confirmed sources. The typical SFR and M_{star} are estimated to be $\simeq 4 M_{\odot} \text{ yr}^{-1}$ and $\simeq 10^8 M_{\odot}$. This yields a relatively high specific SFR of $\simeq 40 \text{ Gyr}^{-1}$ compared to the main sequence at $z = 2 - 6$.
5. We estimate the rest-frame [O III]+ $\text{H}\beta$ EW and obtain the median of $1100_{-730}^{+560} \text{ \AA}$ and $570_{-410}^{+590} \text{ \AA}$ for our NIRCcam- and *HST*-selected galaxies at $z_{\text{spec}} = 8 - 9$, respectively. This is much higher than typical star-forming galaxies at $z \sim 1 - 2$ but consistent with previous photometric-based results at $z \sim 7$ in a similar UV luminosity range. The potential larger EW([O III]+ $\text{H}\beta$) value in the NIRCcam-selected galaxies may indicate these less luminous galaxies are more metal-poor systems than the luminous galaxies, but not extremely metal-poor, where more ionizing photons maintain the EW([O III]+ $\text{H}\beta$) relatively high.
6. We also evaluate ξ_{ion} and find that our NIRCcam- and *HST*-selected galaxies have the median value of $\log(\xi_{\text{ion}}/\text{Hz erg}^{-1}) = 25.77_{-0.43}^{+0.50}$ and $25.47_{-0.23}^{+0.33}$ at $z_{\text{spec}} = 8 - 9$. These median estimates are much higher than typical star-forming galaxies at $z \sim 1 - 2$ but consistent with the recent measurements for the [O III] emitters and Lyman- α emitters at $z = 5 - 7$. The potential higher ξ_{ion} trend in less luminous galaxies indicates the important contributions from faint galaxies to the cosmic reionization, which is consistent with the

empirical model predictions based on $H\alpha$ EW and UV luminosity.

7. We analyze the $[\text{O III}]/H\beta$ line ratio ($= R3$) as a function of M_{star} for the NIRCcam- and *HST*-selected galaxies. We find an increasing trend of $R3$ towards high M_{star} . This trend is opposite to the $z \sim 2 - 3$ results, while it is consistent with the predictions from the simulations because of the high ionization parameter in the early galaxies. With an empirical calibration of the $R3$ method, we evaluate the oxygen abundance and find that these $z = 8 - 9$ galaxies have lower metallicity than $z = 0 - 3$ galaxies at a given M_{star} . This is generally consistent with the current galaxy formation and evolution models.

Software: astropy (Astropy Collaboration et al. 2013), CIGALE (Boquien et al. 2019).

1 We thank Gabriel Brammer for sharing insights into the
 2 NIRSpec data analysis and Takashi Kojima for useful
 3 discussions for this paper. We thank the entire CEERS
 4 team for their effort to design and execute this observa-
 5 tional program, especially the work to design the MSA
 6 observations. This work is based on observations and
 7 archival data made with the *Spitzer Space Telescope*,
 8 which is operated by the Jet Propulsion Laboratory,
 9 California Institute of Technology, under a contract with
 10 NASA, along with archival data from the NASA/ESA
 11 *Hubble Space Telescope*. This research also made use
 12 of the NASA/IPAC Infrared Science Archive (IRSA),
 13 which is operated by the Jet Propulsion Laboratory, Cal-
 14 ifornia Institute of Technology, under contract with the
 15 National Aeronautics and Space Administration. This
 16 project has received funding from NASA through the
 17 NASA Hubble Fellowship grant HST-HF2-51505.001-A
 18 awarded by the Space Telescope Science Institute, which
 19 is operated by the Association of Universities for Re-
 20 search in Astronomy, Incorporated, under NASA con-
 21 tract NAS5-26555.

APPENDIX

A. NON SPEC-Z CONFIRMED SOURCES

In Figure 9 and 10, we show the 1D+2D spectra for the sources not spectroscopically confirmed in this study.

B. CONTINUUM BREAK

In Figure 11, we show the 1D+2D prism spectrum for MPT-ID7 zoomed at around $1\mu\text{m}$. We identify the continuum emission and confirm that the wavelength of the $\text{Ly}\alpha$ continuum break is consistent with what is expected from the redshift determined by the emission lines.

REFERENCES

- | | |
|--|---|
| Adams, N. J., Conselice, C. J., Ferreira, L., et al. 2022,
arXiv e-prints, arXiv:2207.11217 | Amorín, R., Fontana, A., Pérez-Montero, E., et al. 2017,
Nature Astronomy, 1, 0052 |
|--|---|

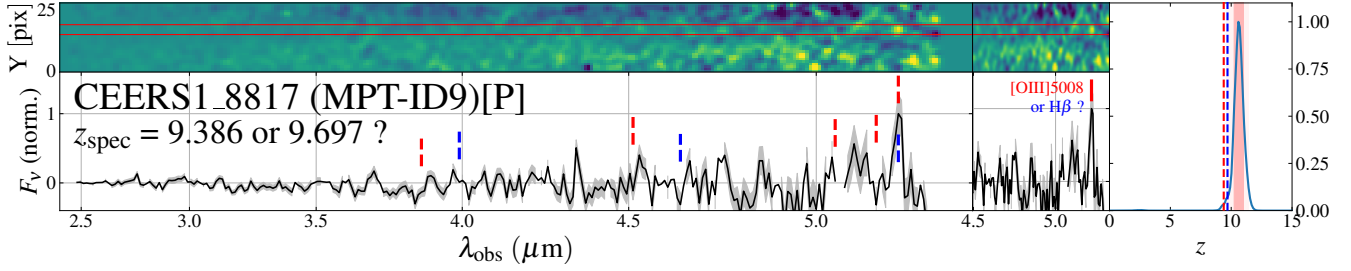


Figure 9. Same as Figure 2, but for MPT-ID9 with the potential single line detection at $5.20 \mu\text{m}$. The red and blue vertical lines indicate the expected wavelengths for the [O III]5008, [O III]4969, $\text{H}\beta$, $\text{H}\gamma$, and [O II]3727, from right to left when the $5.20 \mu\text{m}$ line feature corresponds to [O III]5008 and $\text{H}\beta$, respectively. For the potential line, we rule out the possibility of [O III]4969, because the $3\times$ more bright [O III]5008 line should be detected at the edge of the spectrum in this case. The [O II]3727 at $z = 12.95$ is also unlikely based on $P(z)$.

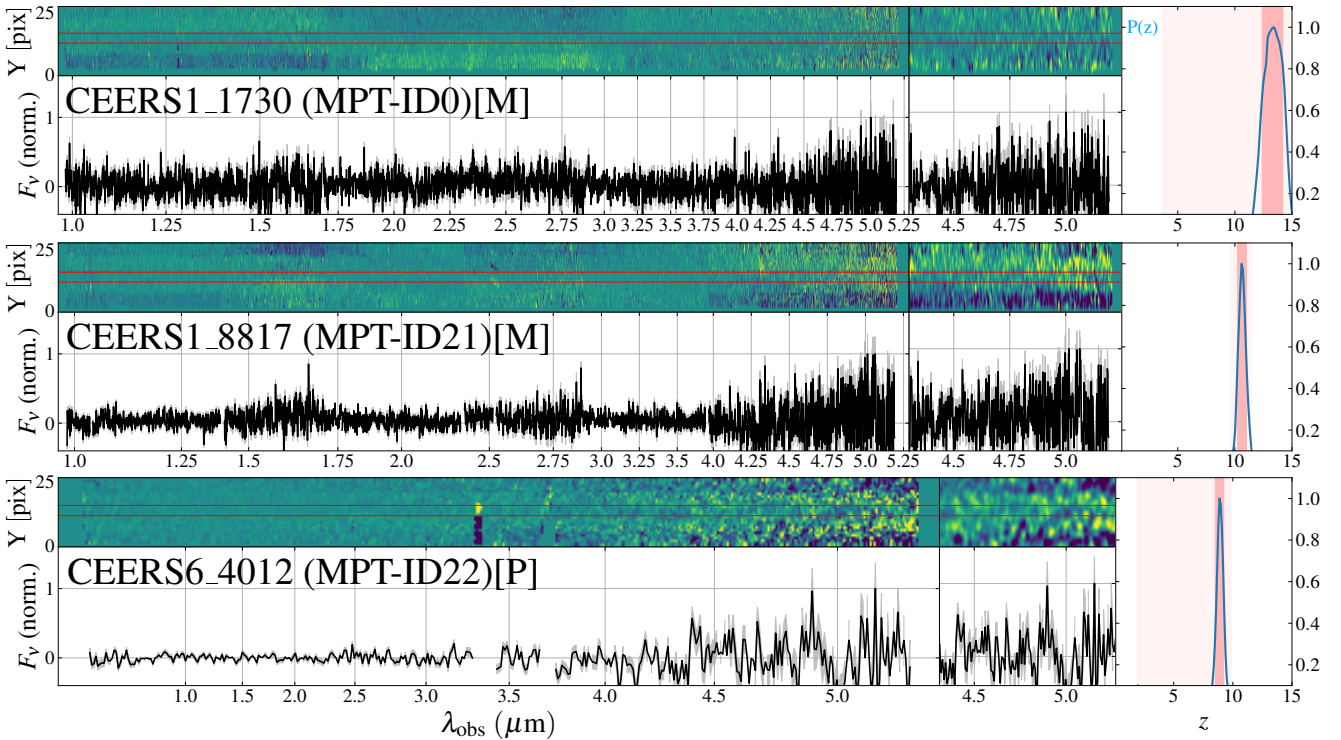


Figure 10. Same as Figure 2, but for MPT-ID0, 21, and 22 without a robust line or continuum detection.

Astropy Collaboration, Robitaille, T. P., Tollerud, E. J., et al. 2013, *A&A*, 558, A33
Atek, H., Shuntov, M., Furtak, L. J., et al. 2022, arXiv e-prints, arXiv:2207.12338
Bagley, M. B., Finkelstein, S. L., Koekemoer, A. M., et al. 2022, arXiv e-prints, arXiv:2211.02495
Bakx, T. J. L. C., Zavala, J. A., Mitsuhashi, I., et al. 2022, arXiv e-prints, arXiv:2208.13642
Behroozi, P., Wechsler, R. H., Hearin, A. P., & Conroy, C. 2019, *MNRAS*, 488, 3143
Behroozi, P., Conroy, C., Wechsler, R. H., et al. 2020, *MNRAS*, 499, 5702

Behroozi, P. S., & Silk, J. 2015, *ApJ*, 799, 32
Beichman, C. A., Rieke, M., Eisenstein, D., et al. 2012, in *Society of Photo-Optical Instrumentation Engineers (SPIE) Conference Series*, Vol. 8442, Space Telescopes and Instrumentation 2012: Optical, Infrared, and Millimeter Wave, ed. M. C. Clampin, G. G. Fazio, H. A. MacEwen, & J. Oschmann, Jacobus M., 84422N
Bhatawdekar, R., Conselice, C. J., Margalef-Bentabol, B., & Duncan, K. 2019, *MNRAS*, 486, 3805
Bian, F., Kewley, L. J., & Dopita, M. A. 2018, *ApJ*, 859, 175

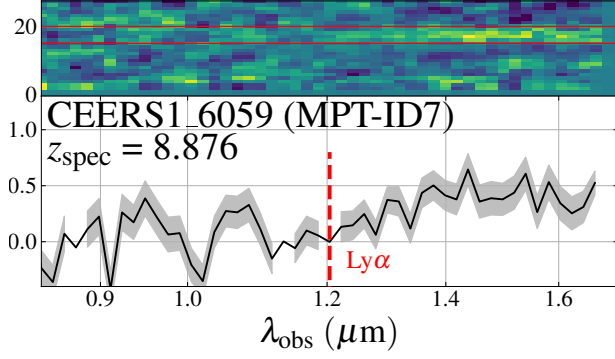


Figure 11. Same as Figure 2, but zoomed at around $\sim 1\mu\text{m}$ of MPT-ID7 whose Lyman- α continuum break is identified in the 1D and 2D spectra. The wavelength of the continuum break is consistent with the emission-line-determined spectroscopic redshift.

- Boquien, M., Burgarella, D., Roehlly, Y., et al. 2019, *A&A*, 622, A103
- Bouwens, R., Illingworth, G., Oesch, P., et al. 2022a, arXiv e-prints, arXiv:2212.06683
- Bouwens, R. J., Smit, R., Labbé, I., et al. 2016, *ApJ*, 831, 176
- Bouwens, R. J., Illingworth, G. D., Oesch, P. A., et al. 2015, *ApJ*, 803, 34
- Bouwens, R. J., Smit, R., Schouws, S., et al. 2021, arXiv e-prints, arXiv:2106.13719
- Bouwens, R. J., Stefanon, M., Brammer, G., et al. 2022b, arXiv e-prints, arXiv:2211.02607
- Boylan-Kolchin, M. 2022, arXiv e-prints, arXiv:2208.01611
- Bradley, L. D., Coe, D., Brammer, G., et al. 2022, arXiv e-prints, arXiv:2210.01777
- Brammer, G. B., van Dokkum, P. G., & Coppi, P. 2008, *ApJ*, 686, 1503
- Burgarella, D., Buat, V., & Iglesias-Páramo, J. 2005, *MNRAS*, 360, 1413
- Calzetti, D., Armus, L., Bohlin, R. C., et al. 2000, *ApJ*, 533, 682
- Castellano, M., Fontana, A., Treu, T., et al. 2022, arXiv e-prints, arXiv:2207.09436
- Chabrier, G. 2003, *PASP*, 115, 763
- Conroy, C., & Gunn, J. E. 2010, *ApJ*, 712, 833
- Curti, M., Cresci, G., Mannucci, F., et al. 2017, *MNRAS*, 465, 1384
- Curti, M., Maiolino, R., Cirasuolo, M., et al. 2020, *MNRAS*, 492, 821
- Curti, M., D'Eugenio, F., Carniani, S., et al. 2022, arXiv e-prints, arXiv:2207.12375
- Curtis-Lake, E., Carniani, S., Cameron, A., et al. 2022, arXiv e-prints, arXiv:2212.04568
- Dahlen, T., Mobasher, B., Faber, S. M., et al. 2013, *ApJ*, 775, 93
- Davé, R., Anglés-Alcázar, D., Narayanan, D., et al. 2019, *MNRAS*, 486, 2827
- Davies, R. L., Förster Schreiber, N. M., Genzel, R., et al. 2021, *ApJ*, 909, 78
- Dayal, P., Choudhury, T. R., Bromm, V., & Pacucci, F. 2017, *ApJ*, 836, 16
- De Barros, S., Oesch, P. A., Labbé, I., et al. 2019, *MNRAS*, 489, 2355
- Developers, J., Averbukh, J., Bradley, L., et al. 2023, doi:10.5281/zenodo.7504710, if you use this software, please cite it as below.
- Ding, X., Onoue, M., Silverman, J. D., et al. 2022, arXiv e-prints, arXiv:2211.14329
- Donnan, C. T., McLeod, D. J., McLure, R. J., et al. 2022a, arXiv e-prints, arXiv:2212.10126
- Donnan, C. T., McLeod, D. J., Dunlop, J. S., et al. 2022b, arXiv e-prints, arXiv:2207.12356
- Eldridge, J. J., & Stanway, E. R. 2009, *MNRAS*, 400, 1019
- Eldridge, J. J., Stanway, E. R., Xiao, L., et al. 2017, *PASA*, 34, e058
- Ellis, R. S., McLure, R. J., Dunlop, J. S., et al. 2013, *ApJ*, 763, L7
- Endsley, R., Stark, D. P., Chevallard, J., & Charlot, S. 2021, *MNRAS*, 500, 5229
- Endsley, R., Stark, D. P., Lyu, J., et al. 2022, arXiv e-prints, arXiv:2206.00018
- Faisst, A. L., Capak, P., Hsieh, B. C., et al. 2016, *ApJ*, 821, 122
- Ferland, G. J., Chatzikos, M., Guzmán, F., et al. 2017, *Rev. Mexicana Astron. Astrofis.*, 53, 385
- Ferrara, A., Pallottini, A., & Dayal, P. 2022, arXiv e-prints, arXiv:2208.00720
- Ferruit, P., Jakobsen, P., Giardino, G., et al. 2022, *A&A*, 661, A81
- Finkelstein, S. L., Ryan, Russell E., J., Papovich, C., et al. 2015, *ApJ*, 810, 71
- Finkelstein, S. L., D'Aloisio, A., Paardekoooper, J.-P., et al. 2019, *ApJ*, 879, 36
- Finkelstein, S. L., Bagley, M. B., Haro, P. A., et al. 2022a, *ApJ*, 940, L55
- Finkelstein, S. L., Bagley, M. B., Ferguson, H. C., et al. 2022b, arXiv e-prints, arXiv:2211.05792
- Fujimoto, S., Finkelstein, S. L., Burgarella, D., et al. 2022a, arXiv e-prints, arXiv:2211.03896
- Fujimoto, S., Ouchi, M., Nakajima, K., et al. 2022b, arXiv e-prints, arXiv:2212.06863
- Giménez-Arteaga, C., Oesch, P. A., Brammer, G. B., et al. 2022, arXiv e-prints, arXiv:2212.08670

- Grogin, N. A., Kocevski, D. D., Faber, S. M., et al. 2011, *ApJS*, 197, 35
- Harikane, Y., Ouchi, M., Oguri, M., et al. 2022, arXiv e-prints, arXiv:2208.01612
- Heintz, K. E., Brammer, G. B., Giménez-Arteaga, C., et al. 2022a, arXiv e-prints, arXiv:2212.02890
- Heintz, K. E., Oesch, P. A., Aravena, M., et al. 2022b, *ApJ*, 934, L27
- Heintz, K. E., Giménez-Arteaga, C., Fujimoto, S., et al. 2022c, arXiv e-prints, arXiv:2212.06877
- Hirschmann, M., Charlot, S., Feltre, A., et al. 2022, arXiv e-prints, arXiv:2212.02522
- Hutchison, T. A., Papovich, C., Finkelstein, S. L., et al. 2019, *ApJ*, 879, 70
- Isobe, Y., Ouchi, M., Nakajima, K., et al. 2023, arXiv e-prints, arXiv:2301.06811
- Iyer, K., Gawiser, E., Davé, R., et al. 2018, *ApJ*, 866, 120
- Iyer, K. G., Gawiser, E., Faber, S. M., et al. 2019, *ApJ*, 879, 116
- Jakobsen, P., Ferruit, P., Alves de Oliveira, C., et al. 2022, *A&A*, 661, A80
- Kannan, R., Springel, V., Hernquist, L., et al. 2022, arXiv e-prints, arXiv:2210.10066
- Khusanova, Y., Le Fèvre, O., Cassata, P., et al. 2020, *A&A*, 634, A97
- Koekemoer, A. M., Faber, S. M., Ferguson, H. C., et al. 2011, *ApJS*, 197, 36
- Labbé, I., Oesch, P. A., Bouwens, R. J., et al. 2013, *ApJ*, 777, L19
- Labbe, I., van Dokkum, P., Nelson, E., et al. 2022, arXiv e-prints, arXiv:2207.12446
- Laporte, N., Nakajima, K., Ellis, R. S., et al. 2017, *ApJ*, 851, 40
- Larson, R. L., Hutchison, T. A., Bagley, M., et al. 2022, arXiv e-prints, arXiv:2211.10035
- Lovell, C. C., Harrison, I., Harikane, Y., Tacchella, S., & Wilkins, S. M. 2022, arXiv e-prints, arXiv:2208.10479
- Ma, X., Hopkins, P. F., Faucher-Giguère, C.-A., et al. 2016, *MNRAS*, 456, 2140
- Mainali, R., Zitrin, A., Stark, D. P., et al. 2018, *MNRAS*, 479, 1180
- Maiolino, R., & Mannucci, F. 2019, *A&A Rev.*, 27, 3
- Maiolino, R., Nagao, T., Grazian, A., et al. 2008, *A&A*, 488, 463
- Mascia, S., Pentericci, L., Calabro', A., et al. 2023, arXiv e-prints, arXiv:2301.02816
- Maseda, M. V., Bacon, R., Lam, D., et al. 2020, *MNRAS*, 493, 5120
- Mason, C. A., Trenti, M., & Treu, T. 2022, arXiv e-prints, arXiv:2207.14808
- Matthee, J., Mackenzie, R., Simcoe, R. A., et al. 2022a, arXiv e-prints, arXiv:2211.08255
- Matthee, J., Sobral, D., Boone, F., et al. 2017, *ApJ*, 851, 145
- Matthee, J., Naidu, R. P., Pezzulli, G., et al. 2022b, *MNRAS*, 512, 5960
- Menci, N., Castellano, M., Santini, P., et al. 2022, *ApJ*, 938, L5
- Morishita, T., & Stiavelli, M. 2022, arXiv e-prints, arXiv:2207.11671
- Naidu, R. P., Matthee, J., Oesch, P. A., et al. 2022a, *MNRAS*, 510, 4582
- Naidu, R. P., Oesch, P. A., van Dokkum, P., et al. 2022b, arXiv e-prints, arXiv:2207.09434
- Nakajima, K., Ouchi, M., Xu, Y., et al. 2022, arXiv e-prints, arXiv:2206.02824
- Nelson, D., Pillepich, A., Springel, V., et al. 2019, *MNRAS*, 490, 3234
- Noll, S., Burgarella, D., Giovannoli, E., et al. 2009, *A&A*, 507, 1793
- Oesch, P. A., Brammer, G., van Dokkum, P. G., et al. 2016, *ApJ*, 819, 129
- Osterbrock, D. E. 1989, *Astrophysics of gaseous nebulae and active galactic nuclei*
- Pallottini, A., Ferrara, A., Gallerani, S., et al. 2022, *MNRAS*, 513, 5621
- Papovich, C., Cole, J., Yang, G., et al. 2022a, arXiv e-prints, arXiv:2301.00027
- Papovich, C., Simons, R. C., Estrada-Carpenter, V., et al. 2022b, *ApJ*, 937, 22
- Pei, Y. C. 1992, *ApJ*, 395, 130
- Pérez-Montero, E., Amorín, R., Sánchez Almeida, J., et al. 2021, *MNRAS*, 504, 1237
- Pontoppidan, K., Blome, C., Braun, H., et al. 2022, arXiv e-prints, arXiv:2207.13067
- Reddy, N. A., Shapley, A. E., Sanders, R. L., et al. 2018, *ApJ*, 869, 92
- Rieke, M. J., Kelly, D., & Horner, S. 2005, in *Society of Photo-Optical Instrumentation Engineers (SPIE) Conference Series*, Vol. 5904, *Cryogenic Optical Systems and Instruments XI*, ed. J. B. Heaney & L. G. Burriesci, 1–8
- Rieke, M. J., Baum, S. A., Beichman, C. A., et al. 2003, in *Society of Photo-Optical Instrumentation Engineers (SPIE) Conference Series*, Vol. 4850, *IR Space Telescopes and Instruments*, ed. J. C. Mather, 478–485
- Rigby, J., Perrin, M., McElwain, M., et al. 2022, arXiv e-prints, arXiv:2207.05632
- Roberts-Borsani, G., Treu, T., Chen, W., et al. 2022, arXiv e-prints, arXiv:2210.15639

- Robertson, B. E., Furlanetto, S. R., Schneider, E., et al. 2013, *ApJ*, 768, 71
- Robertson, B. E., Tacchella, S., Johnson, B. D., et al. 2022, arXiv e-prints, arXiv:2212.04480
- Sanders, R. L., Shapley, A. E., Topping, M. W., Reddy, N. A., & Brammer, G. B. 2023, arXiv e-prints, arXiv:2301.06696
- Sanders, R. L., Shapley, A. E., Reddy, N. A., et al. 2020, *MNRAS*, 491, 1427
- Sanders, R. L., Shapley, A. E., Jones, T., et al. 2021, *ApJ*, 914, 19
- Schaerer, D., Marques-Chaves, R., Oesch, P., et al. 2022, arXiv e-prints, arXiv:2207.10034
- Schaye, J., Crain, R. A., Bower, R. G., et al. 2015, *MNRAS*, 446, 521
- Schmidt, K. B., Huang, K. H., Treu, T., et al. 2017, *ApJ*, 839, 17
- Speagle, J. S., Steinhardt, C. L., Capak, P. L., & Silverman, J. D. 2014, *ApJS*, 214, 15
- Stark, D. P., Walth, G., Charlot, S., et al. 2015, *MNRAS*, 454, 1393
- Stark, D. P., Ellis, R. S., Charlot, S., et al. 2017, *MNRAS*, 464, 469
- Stefanon, M., Bouwens, R. J., Ilingworth, G. D., et al. 2022, *ApJ*, 935, 94
- Tacchella, S., Johnson, B. D., Robertson, B. E., et al. 2022a, arXiv e-prints, arXiv:2208.03281
- Tacchella, S., Finkelstein, S. L., Bagley, M., et al. 2022b, *ApJ*, 927, 170
- Tang, M., Stark, D. P., Chevallard, J., & Charlot, S. 2019, *MNRAS*, 489, 2572
- Tang, M., Stark, D. P., Chen, Z., et al. 2023, arXiv e-prints, arXiv:2301.07072
- Tasca, L. A. M., Le Fèvre, O., Hathi, N. P., et al. 2015, *A&A*, 581, A54
- Treu, T., Roberts-Borsani, G., Bradac, M., et al. 2022, *ApJ*, 935, 110
- Trump, J. R., Arrabal Haro, P., Simons, R. C., et al. 2022, arXiv e-prints, arXiv:2207.12388
- Trussler, J. A. A., Adams, N. J., Conselice, C. J., et al. 2022, arXiv e-prints, arXiv:2207.14265
- Ucci, G., Dayal, P., Hutter, A., et al. 2023, *MNRAS*, 518, 3557
- Vanzella, E., Meneghetti, M., Caminha, G. B., et al. 2020, *MNRAS*, 494, L81
- Wilkins, S. M., Feng, Y., Di-Matteo, T., et al. 2016, *MNRAS*, 458, L6
- Wilkins, S. M., Vijayan, A. P., Lovell, C. C., et al. 2022a, *MNRAS*, 517, 3227
- . 2022b, *MNRAS*, arXiv:2204.09431
- Williams, H., Kelly, P. L., Chen, W., et al. 2022, arXiv e-prints, arXiv:2210.15699
- Yan, H., Ma, Z., Ling, C., et al. 2022, arXiv e-prints, arXiv:2207.11558
- Yoon, I., Carilli, C. L., Fujimoto, S., et al. 2022, arXiv e-prints, arXiv:2210.08413
- Yung, L. Y. A., Somerville, R. S., Finkelstein, S. L., Popping, G., & Davé, R. 2019a, *MNRAS*, 483, 2983
- Yung, L. Y. A., Somerville, R. S., Finkelstein, S. L., et al. 2020a, *MNRAS*, 496, 4574
- Yung, L. Y. A., Somerville, R. S., Popping, G., & Finkelstein, S. L. 2020b, *MNRAS*, 494, 1002
- Yung, L. Y. A., Somerville, R. S., Popping, G., et al. 2019b, *MNRAS*, 490, 2855
- Yung, L. Y. A., Somerville, R. S., Ferguson, H. C., et al. 2022, *MNRAS*, 515, 5416
- Zackrisson, E., Rydberg, C.-E., Schaerer, D., Östlin, G., & Tuli, M. 2011, *ApJ*, 740, 13